J. Fluid Mech (1989), *vol.* 202, *pp.* 43–81
Printed in Great Britain

Spectral evolution of wind-generated surface gravity waves in a dispersed ice field

By D. MASSON† AND P. H. LEBLOND‡
† Institute of Ocean Sciences, Sidney, BC, Canada V8L 4B2
‡ Department of Oceanography, University of British Columbia, 6270 University Boulevard, Vancouver, BC, Canada V6T 1W5

(Received 6 May 1988 and in revised form 19 August 1988)

The Marginal Ice Zone includes wide areas covered by dispersed ice floes in which wave conditions are significantly affected by the ice. When the wind blows from the solid ice pack, towards the open sea, growing waves are scattered by the floes, and their spectral characteristics modified. To further understand this problem, a model for the evolution of wind waves in a sparse field of ice floes has been developed. The sea state is described by a two-dimensional discrete spectrum. Time-limited wave growth is obtained by numerical integration of the energy balance equation using the exact nonlinear transfer integral. Wave scattering by a single floe is represented in terms of far-field expressions of the diffracted and forced potentials obtained numerically by the Green function method. The combined effect of a homogeneous field of floes on the wave spectrum is expressed in terms of the Foldy–Twersky integral equations under the assumption of single scattering. The results show a strong dependence of the spectrum amplitude and directional properties on the ratio of the ice floe diameter to the wavelength. For a certain range of this parameter, the ice cover appears to be very effective in dispersing the energy; the wave spectrum rapidly tends to isotropy, a tendency which prevents the normal growth of wave energy and the decrease in peak frequency. Therefore, in the Marginal Ice Zone, the ability of an offshore wind to generate a significant wave field is severely limited.

1. Introduction

The development of a wind wave spectrum and the nature of the energy terms involved are now understood well enough, in the case of an open ocean, to be able to provide fairly good wave forecasting (e.g. Janssen, Komen & Voogt 1984; Golding 1983). As an extension to the existing theory, it is interesting to examine the situation where waves are generated in the presence of a partial ice cover as encountered in the Marginal Ice Zone (MIZ).

The MIZ is defined as that part of the seasonal ice cover which is close enough to the open ocean boundary to be affected by its presence. It constitutes an active region of dynamic exchanges between sea ice, water and the atmosphere, of which one aspect has not yet been properly investigated, that is wave generation by a wind blowing over the ice field towards the open sea. The presence of scattered ice floes partially covering the sea surface certainly affects the nature of the generated waves, but to what extent? Is the generation process inside the MIZ simply irrelevant or does it lead to waves of significant amplitude by the time the open, ice-free sea is reached? Must wave generation in the MIZ be included in wave climate studies and forecasts?

Most of the previous efforts to study wave–ice interactions in the MIZ have been concentrated on the propagation and attenuation of sea waves and swell entering the ice field (e.g. Wadhams 1973, 1978; Wadhams *et al.* 1986). For this purpose the theory of flexural gravity waves has been used, where the energy of the waves is coupled between an ice layer and the water below it (e.g. Wadhams 1986; Squire 1984). The propagation of these waves and their dispersive behaviour was first analysed for the simplest case of a uniform semi-infinite floating ice sheet, and then extended to wave propagation in a field of discrete floes by representing the floes as successive bands of infinite lateral dimension (Wadhams 1975). In the latter approach, each row transmits and reflects a certain fraction of the incident energy dictated by the transmission properties of the flexural gravity waves on the edge of the band. Although this theory leads to acceptable attenuation rates in most studied cases, it is inadequate. Firstly, as suggested by Robin (1963), the analysis should be different when the horizontal dimension of the ice floes is small compared to the wavelength, in which case, the bending of the floes can be neglected and the floes visualized as rigid floating plates. Also, apart from assuming that typical irregular floes scatter energy only directly backwards, it also ignores diffraction and the wave-making effect of the floes. A more realistic model must describe the ice cover as discrete floes of typical size and shape and attempt to determine the entire scattered wave field due to such floes. To this end, work has been done to obtain detailed measurements of the motion of realistic ice floes in ocean waves (Squire 1983). Using two-dimensional numerical methods developed in naval architecture, he obtained estimates of amplitudes of motion in the different modes of oscillation for individual floes of various shapes. These results can be used to improve the ice-band model previously described but there still remains a need for a more accurate three-dimensional representation in which the scattered wave field could be fully analysed.

All the above mentioned studies have concentrated on the attenuation of ocean waves entering the ice field. However, in this paper, we attempt to investigate the unresolved problem of wave generation in the MIZ itself by suggesting a way in which the partial ice cover may affect the evolution of the wave spectrum. The scattering of the waves is expected to increase the directional spread about the mean direction. The influence of this new energy distribution on the complex nonlinear energy exchange mechanism among waves is a fundamentally interesting aspect of the proposed work. From a more practical point of view, a better knowledge of the wave generation in the MIZ would improve forecasting of wave and ice conditions in a region where these are major environmental hazards, by helping to determine the effective fetch. The results could also be useful in the prediction of the ice edge position and the degree of inhomogeneity in the ice cover.

The next two sections give a detailed description of the model, including a complete derivation of the parameterization of wave–ice interactions. The computed wave-induced motion of the floes and the associated scattering amplitudes are presented in §4. Section 5 describes the numerical simulation method, and the results are given in §6 together with their implications on wind wave evolution inside the MIZ.

2. The energy balance equation

A sea state is commonly represented in terms of its two-dimensional wavenumber spectrum, $F(\boldsymbol{k})$, which is the Fourier transform of the covariance of the surface displacement η at points separated by a distance $\boldsymbol{r}$:

$$F(\boldsymbol{k}) = (2\pi)^{-2}\iint \overline{\eta(\boldsymbol{x})\,\eta(\boldsymbol{x}+\boldsymbol{r})}\exp(-\mathrm{i}\boldsymbol{k}\cdot\boldsymbol{r})\,\mathrm{d}\boldsymbol{r}. \tag{1}$$

Using the linear dispersion relation,

$$(2\pi f)^2 = gk\tanh(kh), \tag{2}$$

(with f the frequency, g the gravitational constant and h the water depth), the corresponding directional frequency spectrum, $F(f,\theta)$, with θ the direction of wave propagation, can be simply related to the wavenumber spectrum by

$$F(f,\theta) = \left[kF(\boldsymbol{k})\frac{\partial k}{\partial f}\right]_{(2\pi f)^2=gk\tanh(kh)} \tag{3}$$

For an ice-free situation, in deep water and in the absence of currents, the spectrum evolves in time t and space $\boldsymbol{x}$ according to the energy balance equation (Hasselmann 1960):

$$\frac{\partial F(f,\theta;\boldsymbol{x},t)}{\partial t}+\boldsymbol{C}_{\mathrm{g}}(f,\theta)\cdot\boldsymbol{\nabla}F(f,\theta;\boldsymbol{x},t) = S_{\mathrm{in}}+S_{\mathrm{ds}}+S_{\mathrm{nl}}, \tag{4}$$

where $\boldsymbol{C}_{\mathrm{g}}(f,\theta)$ is the group velocity, S_{in}, the rate of energy input from the atmosphere, S_{ds} the dissipation rate, mostly through wave breaking, and S_{nl} the energy transfer due to nonlinear interactions among spectral components. In the presence of ice, this energy balance equation will have to be modified to take into account the effects of ice floes on the wave field.

For wave generation by the wind to be of significance, the fraction of the area covered by ice, f_{i}, has to be relatively small ($\leqslant 25\%$, say; this study will provide a more quantitative estimate). Thus, the region of interest for this study is restricted to the outer portion of the ice pack where the ice field is usually composed of randomly distributed small floes with no preferred shape or orientation (e.g. Wadhams 1986).

In the model, the sea surface is assumed to be covered uniformly and sparsely by a random distribution of rigid ice floes. Each mass of floating ice endeavours to follow the displacement of the supporting water surface within limits imposed by its rigidity and inertia. It re-radiates incident wave energy, slightly diminished by dissipative processes in the water and within the ice itself. This scattering effect tends to decrease the energy content of the wave field and, more importantly, to cause a spectral redistribution, spreading out the energy over a broader range of directions. The object of this work is to quantify the modifications due to the partial ice cover on the growing spectrum i.e. to modify the energy terms of (4) for the effect of the ice and to add a new term, S_{ice}, responsible for the extra dissipation and redistribution of energy.

Various models have been developed to obtain the wave growth for a full directional wave spectrum by numerical integration of (4), or some approximation thereof. They differ primarily in the form assumed for the source functions (S_{in}, S_{ds} and S_{nl}) for which a variety of formulations exist, based on theoretical and observational grounds (e.g. Allender *et al.* 1985). The specific form of the input and dissipation terms used in this study is that described by Hasselmann & Hasselmann (1985*a, b*).

The input source function, S_{in}, takes the form proposed by Snyder *et al.* (1981) on the basis of direct measurements of the work done by the atmospheric fluctuations on the waves,

$$S_{\text{in}}(f,\theta) = \begin{cases} 0 & \text{if} \left(\dfrac{U_5 \cos\theta}{c} - 1\right) < 0, \\ 0.25 \dfrac{\rho_{\text{a}}}{\rho_{\text{w}}} \left(\dfrac{U_5 \cos\theta}{c} - 1\right) \omega F(f,\theta) & \text{otherwise,} \end{cases} \tag{5}$$

where ρ_{a} and ρ_{w} are the densities of air and water, respectively, U_5 the wind speed at 5 m, θ the angle between the wind vector and the wave propagation direction, $\omega = 2\pi f$ the wave angular frequency and c the phase velocity.

The less well-known dissipation term, S_{ds}, follows the general form suggested by Hasselmann (1974) for the dissipation due to small-scale white-capping processes. He showed that S_{ds} was to be quasi-linear in the wave spectrum and proportional to the square of the frequency, with a coefficient which depends only on integral spectral parameters:

$$S_{\text{ds}}(f,\theta) = -C\bar{\omega}\left(\frac{\omega}{\bar{\omega}}\right)^2 \left(\frac{\hat{\alpha}}{\hat{\alpha}_{\text{PM}}}\right)^2 F(f,\theta). \tag{6}$$

Here $\hat{\alpha}$ is the integral wave-steepness parameter,

$$\hat{\alpha} = \frac{E\bar{\omega}^4}{g^2},$$

where

$$\bar{\omega} = E^{-1} \int_0^\infty \int_0^{2\pi} F(f,\theta)\, \omega \, \mathrm{d}f \, \mathrm{d}\theta,$$

and

$$E = \int_0^\infty \int_0^{2\pi} F(f,\theta) \, \mathrm{d}f \, \mathrm{d}\theta.$$

The parameter $\hat{\alpha}_{\text{PM}} = 4.57 \times 10^{-3}$ is the theoretical value of $\hat{\alpha}$ for a Pierson–Moskowitz spectrum. The constant C, determining the overall level of dissipation, has been taken from Komen, Hasselmann & Hasselmann (1984) who considered the energy balance for well-developed ocean waves and obtained $C = 3.33 \times 10^{-5}$.

The nonlinear term, S_{nl}, represents the energy exchange between different wave components interacting weakly among themselves, first demonstrated by Phillips (1960). Although these energy transfers are described as 'very weak', this process plays an important role in the evolution of the spectrum. Wave–wave interactions occur among a set of four spectral components when the resonant conditions are satisfied, namely:

$$\boldsymbol{k}_1 + \boldsymbol{k}_2 = \boldsymbol{k}_3 + \boldsymbol{k}_4, \tag{7}$$

and

$$\omega_1 + \omega_2 = \omega_3 + \omega_4, \tag{8}$$

where the wavenumber, in deep water, is related to the angular frequency by the dispersion relation $k_i = \omega_i^2/g$.

Hasselmann (1962) derived an expression for the transfer of energy due to nonlinear interactions by carrying a perturbation analysis to fifth order in a small parameter, the wave slope. From his results, the net rate of change of energy for one spectral component at wavenumber $\boldsymbol{k}_4$ can be computed via the Boltzmann integral expression

$$S_{\mathrm{nl}}(\boldsymbol{k}_4) = \omega_4 \int \dots \int \sigma(\boldsymbol{k}_1, \boldsymbol{k}_2, \boldsymbol{k}_3, \boldsymbol{k}_4)\, \delta(\boldsymbol{k}_1 + \boldsymbol{k}_2 - \boldsymbol{k}_3 - \boldsymbol{k}_4)\, \delta(\omega_1 + \omega_2 - \omega_3 - \omega_4) \\ [n_1 n_2(n_3 + n_4) - n_3 n_4(n_1 + n_2)]\, \mathrm{d}\boldsymbol{k}_1\, \mathrm{d}\boldsymbol{k}_2\, \mathrm{d}\boldsymbol{k}_3, \quad (9)$$

where $n_i(\boldsymbol{k}_i) = F(\boldsymbol{k}_i)/\omega_i$ is the action density and the coupling coefficient σ is a complicated sixth-order homogeneous function of the wavenumbers involved. Equation (9) describes the net energy transfer rate at a given wave component $\boldsymbol{k}_4$ due to interactions with all combinations of four waves satisfying the resonance conditions (7) and (8) represented by the two Dirac δ functions. Because of the extensive computing time required to evaluate the multiple integral of (9), various approximations to the exact expression are commonly used in operational wave models (e.g. Allender *et al.* 1985). Nevertheless, since those parameterizations of S_{nl} have been fitted to standard spectral distributions, they exhibit basic restrictions in their treatment of the nonlinear transfer, and cannot be expected to provide adequate transfer rates for an unusual spectral shape like that anticipated when waves develop in the presence of ice floes. Thus, in this study, the S_{nl} term is computed using the full Boltzmann transfer integral (9). An accurate and fast technique, developed by Hasselmann & Hasselmann (1981, 1985*a*), enables a large number of S_{nl} computations to be carried out, as required for this work. The method, based on a symmetrical treatment of the interactions, is one to two orders of magnitude more efficient than previous ones. This is mainly achieved by exploiting the invariance of the coupling coefficient σ with respect to permutations of the wavenumbers, and the principle of detailed balance by which the computation of the change in action density for one wavenumber gives also the identical action changes (except for a simple sign rule) for the other three components participating in a given interaction.

Now that the three energy terms of (4) have been satisfactorily defined, the effect of a partial ice cover may be introduced. First, because waves can neither be generated by the wind nor dissipated by the usual breaking mechanisms in that fraction f_{i} of the sea surface covered by ice, both S_{in} and S_{ds} are reduced by a factor $(1-f_{\mathrm{i}})$ from their ice-free values given above. There remains the determination of the new term, S_{ice}, which parameterizes the scattering and extra dissipation of energy by the ice.

3. Modelling the partial ice cover

The determination of the additional source term, S_{ice}, consists of analysing the scattering of a random wave field described by its energy spectrum, $F(f, \theta)$, incident on a random array of ice floes. Assuming that each discrete component of the spectrum interacts independently with the floes, two aspects of the problem may be distinguished. First, the ability of a single floe to scatter a certain fraction of the incident energy associated with a single spectral component is considered in §3.1. Secondly, the average wave field due to scattering of this wave by the whole array of ice floes is computed. The directional scattered spectrum, for each frequency, is then obtained by summing the contributions from the incident and scattered waves of all directions (§3.2). Finally, the dissipation of energy due to the presence of the partial ice cover is evaluated (§3.3).

3.1. *Scattering of a plane wave by a single floe*

There are two distinct approaches to solving the hydrodynamic problem of a floating body in waves: Morison's equation and potential flow theory (e.g. Garrison 1978). These two procedures have their own limits of applicability. The former considers the flow past a body with velocity and acceleration such as would occur at its centre if it were not present and, therefore, is valid for objects which are small in relation to the wavelength. On the other hand, when the body size to wavelength ratio, D/L, is sufficiently large ($\geqslant 0.2$), the incident wave undergoes important scattering (or diffraction) and the more explicit potential theory is required to describe the flow. Finally, both approaches are limited by the value of the wave height to wavelength ratio, H/L, steep waves being affected by nonlinear effects (with $(H/L)_{\max} \approx 0.14$ in deep water).

In the region studied, the outer part of the MIZ, both ocean and wind act on the ice cover to form heavily rafted and ridged small floes (e.g. Bauer & Martin 1980). These are represented, in the model, by truncated cylinders of diameter $15 \leqslant D \leqslant 50$ m and draft $1 \leqslant d \leqslant 4$ m. The geometry of one individual floe can not be fully described by such a simple shape. Sharp corners, for example, would cause flow separation, increasing form drag. However, the overall effect of the ice field on the energy distribution of the growing waves should be properly derived using this simple representation. Within that given range of floe diameters and for the expected values of wavelength in the early stage of this short fetch situation ($L \leqslant 60$ m), the value of the parameter D/L remains in the region of validity of the potential flow theory. Therefore, in this work, potential flow theory is used rather than the Morison equation.

Assuming the fluid incompressible and the flow irrotational, the problem reduces to the determination of a velocity potential, Φ, which satisfies the Laplace equation, $\nabla^2\Phi = 0$. The function Φ is defined here such that $\boldsymbol{u} = \nabla\Phi$, with $\boldsymbol{u}$ the fluid velocity vector. The analysis is based on the assumption that the amplitude of the wave is small. Through linearization, the scattering process can be decomposed and treated as the sum of two distinct mechanisms: the fluid motion produced by a body forced to oscillate in otherwise still water and the interaction of a regular wave with a restrained body (e.g. Sarpkaya & Isaacson 1981). Because of its symmetry relative to the vertical axis, a floating cylinder will be forced by an incident plane wave to oscillate in three degrees of freedom only: surge, back and forth in the direction of the incident wavenumber $\boldsymbol{k}$; heave, up and down; and pitch, about an axis parallel to the wave crests. For each mode, the resulting small periodic motion, of angular freqency ω, may be expressed in the form $\xi_b \mathrm{e}^{-\mathrm{i}\omega t}$ where ξ_b is the complex amplitude for the mode of motion b, with $b = 1$, 2 and 3 corresponding to surge, heave and pitch respectively (figure 1). In linearizing the problem, the velocity potential, also harmonic, can be obtained by superposition of 5 components:

$$\Phi = \mathrm{Re}\left(\left[\phi_0 + \phi_4 + \sum_{b=1}^{3} \xi_b \phi_b\right]\mathrm{e}^{-\mathrm{i}\omega t}\right), \tag{10}$$

where ϕ_0 is the undisturbed part of the incident wave potential, ϕ_4 the diffracted potential, ϕ_b, for $b = 1, \ldots, 3$, the forced potentials and Re( ) indicates the real part.

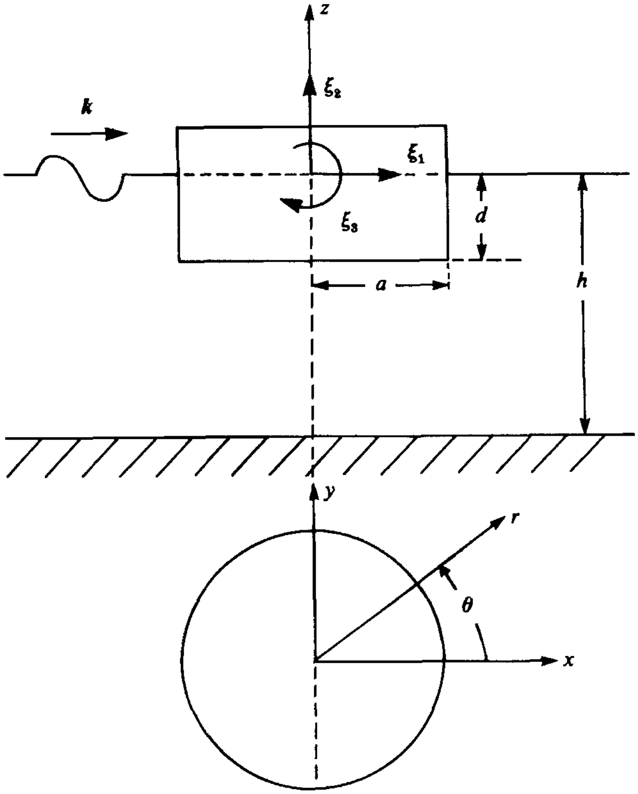

FIGURE 1. Cylindrical floe of radius $a = \frac{1}{2}D$ and draft d in water of depth h. The three modes of motion have amplitudes of ξ_i, with subscript: 1 for surge, 2 for heave and 3 for pitch. Here (x, y, z) form a Cartesian coordinate system and (r, θ, z) the corresponding cylindrical coordinate system.

The potential associated with an incident plane wave, of amplitude $\frac{1}{2}H$, in water of finite depth, is usually given as

$$\phi_0 = -\frac{igH}{2\omega}\frac{\cosh[k(z+h)]}{\cosh(kh)}e^{ikx}, \tag{11}$$

where x is measured in the direction of wave propagation and z vertically upwards from the still water level. It is more convenient, here, to use a cylindrical coordinate system with r measured radially from the z-axis and θ counterclockwise from the positive x-axis (figure 1). The incident potential then takes the form

$$\phi_0 = -\frac{igH}{2\omega}\frac{\cosh[k(z+h)]}{\cosh(kh)}\sum_{l=0}^{\infty}\beta_l J_l(kr)\cos(l\theta), \tag{12}$$

where
$$\beta_l = \begin{cases} 1 & \text{if } l = 0, \\ 2i^l & \text{otherwise,} \end{cases}$$

and J_l is the Bessel function of the first kind of order l.

The complex potentials of (10) must satisfy the Laplace equation and the usual linearized boundary conditions at the seabed, free surface, far field, and the condition to be applied on the equilibrium surface of the floating body, S_0,

$$\frac{\partial(\phi_0+\phi_4+\Sigma_{b=1}^{3}\xi_b\phi_b)}{\partial \boldsymbol{n}} = v_n = \sum_{b=1}^{3} -\mathrm{i}\omega\xi_b n_b \quad \text{on } S_0, \tag{13}$$

where $\boldsymbol{n}$ is the unit vector in the direction normal to S_0, directed outward from the body and v_n the magnitude of the velocity of the surface in that direction, given by $V_n = \mathrm{Re}(v_n \mathrm{e}^{-\mathrm{i}\omega t})$. V_n is the sum of the surge, heave and pitch components with $n_1 = n_x$, $n_2 = n_z$ and $n_3 = zn_x - xn_z$ where n_x, n_y and n_z are the direction cosines of $\boldsymbol{n}$ with respect to the x-, y- and z-directions respectively.

This boundary-value problem is solved using the Green function method. In the usual way (e.g. Wehausen & Laitone 1960), the unknown potentials, $\phi_b(\boldsymbol{x})$, are expressed in terms of a surface distribution of sources

$$\phi_b(\boldsymbol{x}) = \frac{1}{4\pi}\int_{S_0} f_b(\boldsymbol{X})\, G(\boldsymbol{x},\boldsymbol{X})\,\mathrm{d}S \quad \text{for } b = 1,\ldots,4, \tag{14}$$

where $f_b(\boldsymbol{X})$ is a source distribution function at $\boldsymbol{X} = (X,Y,Z)$, a point on S_0, and $G(\boldsymbol{x},\boldsymbol{X})$ a Green function for the general point $\boldsymbol{x}$ due to a source of unit strength at $\boldsymbol{X}$.

The source strength distribution function, $f_b(\boldsymbol{X})$, and the amplitude of motion, ξ_b, for each mode b, are obtained using a method described by Isaacson (1982) and of which the broad outlines are given here. Because of the body's axisymmetry, various functions may be expressed as Fourier series in the angle about the body's vertical axis, θ, reducing considerably the computational effort required from that for bodies of arbitrary shape. In finite depth, the appropriate Green function that satisfies the Laplace equation, the boundary conditions on the ocean floor and at the free surface, and the radiation condition, first derived by John (1950), was given in a symmetrical form by Fenton (1978):

$$G = \sum_{l=0}^{\infty}\left(\sum_{m=0}^{\infty} G_{lm}\right)(2-\delta_{l0})\cos[l(\theta-\Theta)], \tag{15}$$

where δ_{l0} is the Kronecker delta,

$$G_{lm} = 4C_m \cos[\mu_m(Z+h)]\cos[\mu_m(z+h)]\,K_l\begin{pmatrix}\mu_m r\\ \mu_m R\end{pmatrix} I_l\begin{pmatrix}\mu_m R\\ \mu_m r\end{pmatrix},$$

$$C_m = \frac{\mu_m^2+\nu^2}{(\mu_m^2+\nu^2)\,h-\nu},$$

and the cylindrical coordinates (R,Θ,Z) correspond to the point (X,Y,Z) on the surface S_0. I_l and K_l are the modified Bessel functions of order l of the first and second kinds, respectively, with the upper of the alternative arguments used if $r \geqslant R$ and the lower otherwise. Also, $\nu = \omega^2/g$ and μ_m are the roots of

$$\mu_m h \tan(\mu_m h) = -\nu h, \tag{16}$$

with μ_0 the imaginary root ($\mu_0 = -\mathrm{i}k$), and, for $m \geqslant 1$, μ_m the positive real roots in ascending order.

The source strength distribution function of (14), for each mode of oscillation b, is expanded as:

$$f_b(\boldsymbol{X}) = \sum_{l=0}^{\infty} f_{bl}(s)\cos(l\Theta), \tag{17}$$

where $s(r,z)$ is the distance measured along the body contour in a vertical plane. The coefficients $f_{bl}(s)$ are determined by the boundary condition (13) applied on s_0, the equilibrium body contour, discretized into a finite number N of short segments, with $f_{bl}(s)$ assumed uniform over each segment. The various results, presented in §4, were calculated using $15 \leqslant N \leqslant 30$. The body motion amplitudes, ξ_b, are then obtained from the equation of motion for a freely floating axisymmetric body. These two parameters, $f_{bl}(s)$ and ξ_b, had to be computed for each particular floe shape used in the model.

Once the source strength distribution functions and the amplitudes of motion, for each floe configuration, have been solved for by the method described above (see Isaacson (1982) for more details on the procedure), an expression for the potential Φ at any point in the fluid can be derived. Substituting (15) and (17) into (14), each scattered (forced and diffracted) potential can be written as

$$\phi_b(r,\theta,z) = \frac{1}{4\pi}\int_{S_0} \sum_{l=0}^{\infty} f_{bl}(s)\cos(l\Theta)\left(\sum_{m=0}^{\infty} G_{lm}\right)(2-\delta_{l0})\cos[l(\theta-\Theta)]\,\mathrm{d}S. \tag{18}$$

Expressing $\mathrm{d}S$ as $R\,\mathrm{d}\Theta\,\mathrm{d}s$, and integrating with respect to Θ, (18) becomes

$$\phi_b(r,\theta,z) = \frac{1}{2}\sum_{l=0}^{\infty}\int_{s_0} f_{bl}(s)\left(\sum_{m=0}^{\infty} G_{lm}\right)\cos(l\theta)\,R\,\mathrm{d}s. \tag{19}$$

Introducing in (19) the discretization of s_0 previously mentioned, the integral over s_0 is replaced by a finite sum over N segments of length L_j:

$$\phi_b(r,\theta,z) = \frac{1}{2}\sum_{l=0}^{\infty}\sum_{j=1}^{N} f_{bl}(s_j)\sum_{m=0}^{\infty} G_{lm}(r,z,R_j,Z_j)\cos(l\theta)\,R_j L_j. \tag{20}$$

For large r, the Bessel function, $K_l(\mu_m r)$, of (15) takes the asymptotic form (e.g. Abramowitz & Stegun 1965)

$$\lim_{r\to\infty} K_l(\mu_m r) = \left(\frac{\pi}{2\mu_m r}\right)^{\frac{1}{2}} \mathrm{e}^{-\mu_m r} + O(r^{-\frac{3}{2}}). \tag{21}$$

It follows that the potential (20), at large distance from the body, is dominated by the $m = 0$ term, the terms for which $m \geqslant 1$ dying out exponentially (the roots $(\mu_m)_{m\geqslant 1}$ being real). The far field expression for (20) is then

$$\lim_{r\to\infty} \phi_b(r,\theta,z) = \frac{1}{2}\sum_{l=0}^{\infty}\sum_{j=1}^{N} f_{bl}(s_j)\,G_{l0}(r,z,R_j,Z_j)\cos(l\theta)\,R_j L_j + O(r^{-\frac{3}{2}}), \tag{22}$$

with

$$G_{l0}(r,z,R_j,Z_j) = \left\{2\left(\frac{2\pi}{k}\right)^{\frac{1}{2}} \mathrm{i}C_0 \cosh[k(Z_j+h)]\cosh[k(z+h)]\,\mathrm{e}^{-\frac{1}{4}\mathrm{i}\pi-\frac{1}{2}\mathrm{i}\pi l} J_l(kR_j)\right\}\frac{1}{r^{\frac{1}{2}}}\mathrm{e}^{\mathrm{i}kr},$$

and

$$C_0 = \frac{\nu^2-k^2}{(\nu^2-k^2)\,h-\nu}.$$

In (22), the term corresponding to the so-called local waves decays as $r^{-\frac{3}{2}}$. Finally, the surface displacement, for each mode b, at large distance from the floe, is obtained from the velocity potential of (22), using the linearized dynamic boundary condition at $z = 0$

$$\eta_b(r,\theta,t) \approx \mathrm{Re}\left(A\tfrac{1}{2}HD_b(\theta)\frac{1}{r^{\frac{1}{2}}}\mathrm{e}^{\mathrm{i}(kr-\omega t)}\right), \tag{23}$$

with, for $b = 1, \dots 3$,

$$D_b(\theta) = -\frac{\omega}{g}\frac{\xi_b}{\frac{1}{2}H}\left(\frac{2\pi}{k}\right)^{\frac{1}{2}} C_0 \cosh(kh)\,\mathrm{e}^{-\frac{1}{4}\mathrm{i}\pi} \sum_{j=1}^{N} \sum_{l=0}^{\infty} f_{bl}(s_j) \cosh[k(Z_j+h)] \times J_l(kR_j)\,\mathrm{e}^{-\frac{1}{2}\mathrm{i}\pi l} R_j L_j \cos(l\theta),$$

and, for the diffracted wave ($b = 4$),

$$D_4(\theta) = -\frac{\omega}{g}\frac{1}{\frac{1}{2}H}\left(\frac{2\pi}{k}\right)^{\frac{1}{2}} C_0 \cosh(kh)\,\mathrm{e}^{-\frac{1}{4}\mathrm{i}\pi} \sum_{j=1}^{N} \sum_{l=0}^{\infty} f_{bl}(s_j) \cosh[k(Z_j+h)] \times J_l(kR_j)\,\mathrm{e}^{-\frac{1}{2}\mathrm{i}\pi l} R_j L_j \cos(l\theta),$$

and A is a factor introduced to conserve energy, as explained below. In (23), the surface displacements describe cylindrical waves radiating away from the floe with an amplitude of $(\frac{1}{2}AHD_b(\theta)\frac{1}{r^{\frac{1}{2}}})$ as a function of the direction of propagation θ and distance r.

In the Appendix, the infinite depth expression for the scattering amplitude, $D_b(\theta)$, is derived. In the case of large depth, the Green function of (15) takes a different form, first obtained by John (1950). As one would expect, the finite depth $D_b(\theta)$ of (23) tends to the one obtained in deep water, (A 11), by letting $kh \to \infty$. The details need not be given here, however.

The scattering amplitude of (23) (or (A 11)) gives the amplitude and the directional properties of the four scattered waves. Also, the total scattering cross-section of a floe, defined as

$$\sigma_s = \sum_{b=1}^{4} \int_0^{2\pi} |D_b(\theta)|^2\,\mathrm{d}\theta, \tag{24}$$

determines the fraction of the incident energy being scattered through diffraction and the forced motions. As will be seen in the next section, the ability of a particular ice field to disperse energy over all directions strongly depends on the effectiveness of these two processes.

3.2. *Scattering by the entire ice field*

So far, the problem of a plane wave incident on a single floe has been investigated. However, the required wave field is determined by the scattering of each spectral component on the whole array of randomly distributed floes. To obtain this wave field, a statistical average of the scattered waves is done over the entire domain using the theory of wave propagation and scattering in random media.

Since the floes are randomly distributed, the scattered field is not constant and its amplitude and phase fluctuate in a random manner. The total wave field can be divided into the average field, $\langle\eta(\boldsymbol{r},t)\rangle$, also called the coherent field, and the fluctuating field, $\eta_f(\boldsymbol{r},t)$, called the incoherent field. At a point $\boldsymbol{r}_a$ on the ocean surface, the surface displacement is the sum of the incident wave and the contributions from all the scatterers located at $\boldsymbol{r}_s$. The spatially averaged (ergodically equivalent to the ensemble averaged) wave at $\boldsymbol{r}_a$, $\langle\eta(\boldsymbol{r}_a,t)\rangle$, is given by the Foldy–Twersky integral equation (e.g. Ishimaru 1978)

$$\langle\eta(\boldsymbol{r}_a,t)\rangle = \eta_0(\boldsymbol{r}_a,t) + \iint u_s^a \langle\eta(\boldsymbol{r}_s,t)\rangle\,\rho(\boldsymbol{r}_s)\,\mathrm{d}\boldsymbol{r}_s, \tag{25}$$

where $\eta_0(\boldsymbol{r}_a,t)$ is the incident wave at $\boldsymbol{r}_a$, $u_s^a\langle\eta(\boldsymbol{r}_s,t)\rangle$ a symbolic notation to indicate the wave at $\boldsymbol{r}_a$ due to the scattering of the coherent wave, $\langle\eta(\boldsymbol{r}_s,t)\rangle$, incident on a scatterer located at $\boldsymbol{r}_s$, and $\rho(\boldsymbol{r}_s)$ the number of floes per unit area, also called 'number' density.

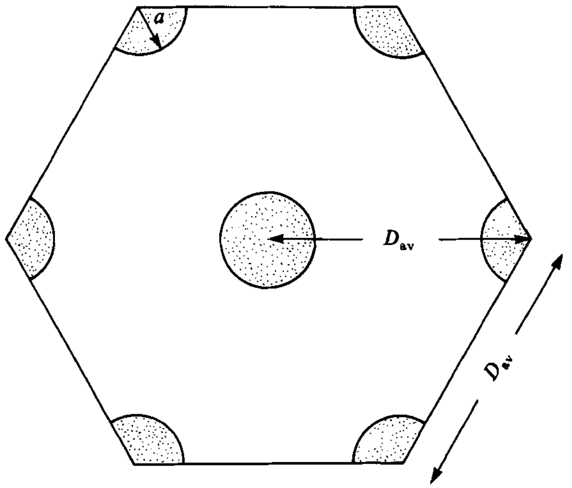

FIGURE 2. Simple hexagonal model of a homogeneous ice cover. D_{av} is the average distance between floes of radius a.

Because of the finite size of the floes and to prevent divergence of the integral in (25), a decay of the number density with distance from $\boldsymbol{r}_a$ must be included to account for shading of remote scatterers by nearby floes. A homogeneous field of ice floes could be represented by a simple hexagonal model in which the floes are separated by D_{av}, the average distance between floes (figure 2). The polygon includes a total of three floes and covers a surface $S = \frac{3}{2}\sqrt{3}D_{av}^2$. Thus, without shading, the uniform number density is

$$\rho_0 = \frac{3}{S} = \frac{2}{\sqrt{3}D_{av}^2}. \tag{26}$$

The shading is introduced by considering the effect of a ring of average radius r and of small width $dr = 2a$. The fraction of the perimeter of this ring taken by ice floes is

$$f' = \frac{\rho_0(2\pi r\, 2a)\, 2a}{2\pi r} = \frac{8a^2}{\sqrt{3}D_{av}^2}, \tag{27}$$

and is independent of r. The transmittivity of each ring of width $2a$, assuming opaque floes, is then

$$T_r = (1-f') = \left(1-\frac{8a^2}{\sqrt{3}D_{av}^2}\right). \tag{28}$$

On a distance $r = |\boldsymbol{r}_s-\boldsymbol{r}_a|$ from the centre of a floe located at $\boldsymbol{r}_a$, waves scattered at $\boldsymbol{r}_s$ will travel through $(r-a)/2a$ rings before reaching $\boldsymbol{r}_a$. Therefore, under the single scattering approximation where the amplitude of a wave scattered more than once is assumed to be negligible, the number of floes per unit area effectively radiating waves to $\boldsymbol{r}_a$, without being shaded by other floes, is given by

$$\rho_e(r) = \rho_0(T_r)^{(r-a)/2a} = \frac{2}{\sqrt{3}D_{av}^2(1-8a^2\sqrt{3}D_{av}^2)^{\frac{1}{2}}}\left(1-\frac{8a^2}{\sqrt{3}D_{av}^2}\right)^{r/2a}. \tag{29}$$

This 'effective' number density, $\rho_e(r)$, decreases with distance at a rate which is a function of the degree of ice cover, $f_i = 2\pi a^2\sqrt{3}D_{av}^2$, with the importance of the contributions from nearby floes in the integral of (25) increasing with f_i (figure 3).

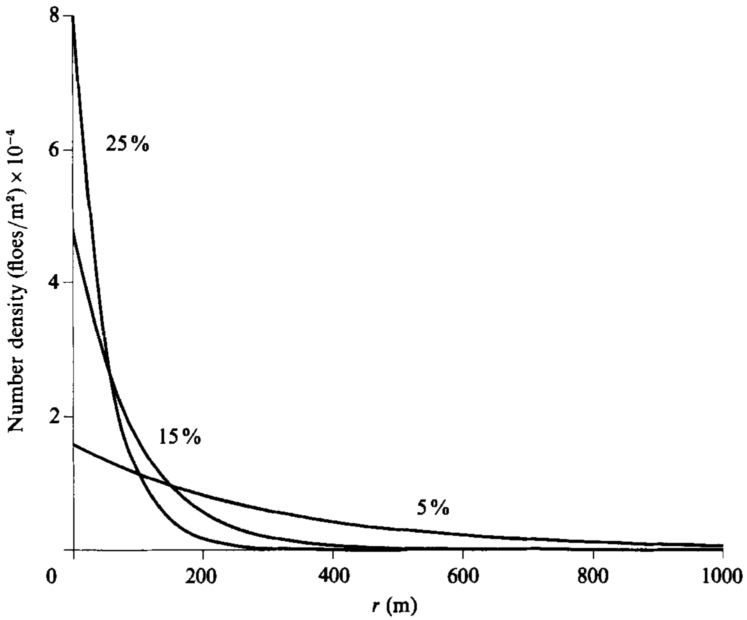

FIGURE 3. Effective number density, $\rho_e(r)$, for different degree of ice cover, f_i. In this example, the floes have a radius $a = 10$ m.

To obtain an expression for the average wave field, (25) is solved by first neglecting multiple scattering:

$$u_s^a\langle\eta(\boldsymbol{r}_s,t)\rangle \approx u_s^a\,\eta_0(\boldsymbol{r}_s,t). \tag{30}$$

Secondly, since the waves travel through a sparse distribution of scatterers, the far field approximation obtained in (23) is used to give

$$u_s^a\,\eta_0(\boldsymbol{r}_s,t) \approx \mathrm{Re}\left(A\tfrac{1}{2}H\sum_{b=1}^{4} D_b(\theta)\frac{1}{r^{\frac{1}{2}}}\mathrm{e}^{\mathrm{i}(kr-\omega t)}\right), \tag{31}$$

where θ is the angle between the incident direction and $r = |\boldsymbol{r}_a - \boldsymbol{r}_s|$. Equation (31) is valid only when $\langle\eta(\boldsymbol{r}_s,t)\rangle$ can be approximated by $\eta_0(\boldsymbol{r}_s,t)$, and when $\boldsymbol{r}_a$ is in the far zone of the floe at $\boldsymbol{r}_s$. These two assumptions may seem restrictive but, in the present model of low ice concentration, it appears reasonable to assume that the amplitude of a wave scattered more than once is negligible compared to the ones included in the simple scattering theory, and to neglect the local waves. About this last assumption, it is interesting to examine the relative amplitude of the neglected waves. In (22), or (A 10), the local waves decay as $(r^{-\frac{3}{2}})$. As previously mentioned, the importance of the contributions from floes located at small r increases with f_i. Then, referring to the values of the effective number density, $\rho_e(r)$, for $f_i = 0.25$ (figure 3), one has to go as far as $r' \approx 21$ m to have the equivalent of one complete floe effectively radiating waves;

$$\int_0^{2\pi}\int_0^{r'} \rho_e(r)\,r\,\mathrm{d}r\,\mathrm{d}\theta = 2\pi\int_0^{r'}\rho_e(r)\,r\,\mathrm{d}r \approx 1 \quad \text{for } r' = 21 \text{ m}.$$

At this distance, the local wave amplitude is less than 5% of the far-field wave amplitude. For larger ice floes ($a > 10$ m), r' has even larger values, resulting in a smaller relative amplitude ($<5\%$) of the neglected local waves. Thus, in this model, for an ice concentration $f_i \leqslant 0.25$, the contribution to the scattered energy from the waves neglected by the far-field approximation is small and can be safely neglected.

To solve (25) it is more convenient to use the Cartesian coordinates (x, y) with x in the direction of the incident wave. Since the geometry of the ice field is independent of y, the coherent field must also be independent of y and should behave as plane waves propagating along the x-axis. Waves scattered in other directions are then included in the incoherent field. Using the approximations (30) and (31), (25) becomes

$$\langle \eta(x_a, t)\rangle = \eta_0(x_a, t) + \mathrm{Re}\left(\tfrac{1}{2}AH\left[\underbrace{\iint_{-\infty}^{+\infty} D(\theta)\frac{1}{r^{\frac{1}{2}}}\mathrm{e}^{\mathrm{i}kr}\rho_e(r)\,\mathrm{d}y_s\,\mathrm{d}x_s}_{\mathrm{II}}\right]\mathrm{e}^{-\mathrm{i}\omega t}\right), \tag{32}$$

with
$$r = \left((x_a - x_s)^2 + (y_a - y_s)^2\right)^{\frac{1}{2}},$$

and
$$D(\theta) = \sum_{b=1}^{4} D_b(\theta).$$

The integral over y_s of (32) is evaluated by the method of stationary phase (e.g. Jeffreys 1962) with the stationary point $y_0 = y_a$. From the general form of the asymptotic solution obtained by this method, the integral becomes (Masson 1987)

$$\mathrm{II} \approx \begin{cases} \left(\dfrac{2\pi}{k}\right)^{\frac{1}{2}} \exp(\tfrac{1}{4}\mathrm{i}\pi)\, D(0) \exp(\mathrm{i}k(x_a - x_s))\, \rho_e(x_a - x_s) & \text{if } x_s < x_a \\[2ex] \left(\dfrac{2\pi}{k}\right)^{\frac{1}{2}} \exp(\tfrac{1}{4}\mathrm{i}\pi)\, D(\pi) \exp(\mathrm{i}k(x_s - x_a))\, \rho_e(x_s - x_a) & \text{if } x_a < x_s. \end{cases} \tag{33}$$

Using (33), the coherent field of (32) can now be written as

$$\begin{aligned} \langle \eta(x_a, t)\rangle = {} & \\ & \eta_0(x_a, t) + \mathrm{Re}\left(\tfrac{1}{2}AH\left(\frac{2\pi}{k}\right)^{\frac{1}{2}} \exp(\tfrac{1}{4}\mathrm{i}\pi)\left[\left\{\int_{-\infty}^{x_a} \exp(-\mathrm{i}kx_s)\,\rho_e(x_a - x_s)\,\mathrm{d}x_s\right\} D(0)\exp(\mathrm{i}kx_a)\right.\right. \\ & \left.\left. + \left\{\int_{x_a}^{\infty} \exp(\mathrm{i}kx_s)\,\rho_e(x_s - x_a)\,\mathrm{d}x_s\right\} D(\pi)\exp(-\mathrm{i}kx_a)\right]\exp(-\mathrm{i}\omega t)\right). \end{aligned} \tag{34}$$

The last expression for the coherent field, valid for any x_a, can be simplified by choosing a centred observation point, with $x_a = 0$. Using the effective number density of (29), (34) becomes

$$\langle \eta(x_a = 0, t)\rangle = \eta_0(x_a = 0, t) + \mathrm{Re}\,(\tfrac{1}{2}AH\,\alpha_c[D(0)\,\mathrm{e}^{\mathrm{i}k(0)} + D(\pi)\,\mathrm{e}^{-\mathrm{i}k(0)}]\,\mathrm{e}^{-\mathrm{i}\omega t}), \tag{35}$$

with the 'coherent scattering' coefficient, α_c, given as

$$\alpha_c = \left(\frac{2\pi}{k}\right)^{\frac{1}{2}} \exp(\tfrac{1}{4}\mathrm{i}\pi)\frac{2}{\sqrt{3}D_{av}^2\left(1 - \dfrac{8a^2}{\sqrt{3}D_{av}^2}\right)^{\frac{1}{2}}}\int_0^{\infty} \exp(\mathrm{i}kx_s)\left(1 - \frac{8a^2}{\sqrt{3}D_{av}^2}\right)^{x_s/2a}\mathrm{d}x_s.$$

In (35), the resultant average field is made up of three components: the incident wave, $\eta_0(x_a, t)$, to which has been added a wave travelling in the same direction and of amplitude proportional to $D(0)$, and a second one travelling in the opposite direction, of amplitude proportional to the backward scattering amplitude, $D(\pi)$. In

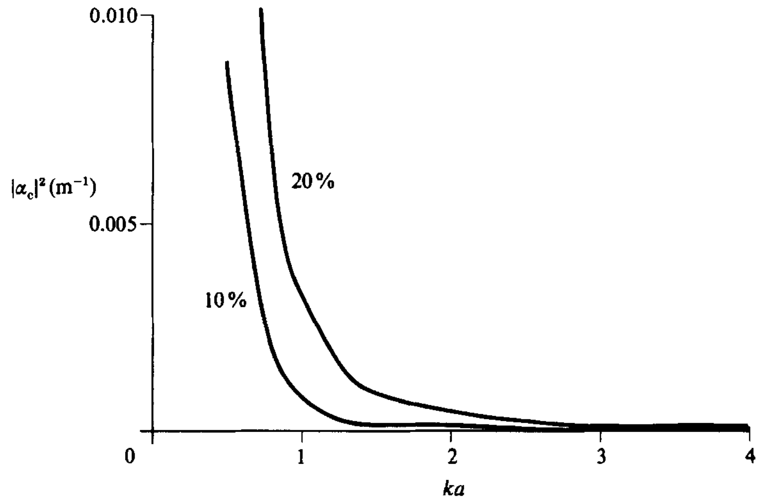

FIGURE 4. The square of the modulus of the coherent scattering coeffient, $|\alpha_c|^2$, as a function of the parameter ka. Results are given for floes of radius $a = 10$ m and ice concentration $f_i = 0.1$ and 0.2.

other words, the only scattered waves interfering in a 'coherent' way to be a component of the average field are the ones generated in the ± incident direction. The square of the magnitude of the coherent scattering coefficient, $|\alpha_c|^2$, which determines the amount of energy associated with these waves, decreases rapidly with the parameter ka (figure 4).

Because of the randomness of the ice floe distribution, the phases of waves scattered by different floes have no correlation among themselves. Therefore, their contributions to the total energy of the scattered wave field can be simply added regardless of their relative phases. The total intensity is then the average of the square of the magnitude of the total field, and is the sum of the coherent intensity, $|\langle\eta(x_a,t)\rangle|^2$, associated with the coherent field, and the incoherent intensity, $\langle|\eta_f(\boldsymbol{r}_a,t)|^2\rangle$, the energy of the fluctuating field.

Accordingly, the energy distribution from the scattering of a single component of the incident spectrum is obtained from Twersky's integral equation for the total intensity, similar to the Foldy–Twersky integral equation (25) for the coherent field,

$$\langle|\eta(\boldsymbol{r}_a,t)|^2\rangle = |\langle\eta(x_a,t)\rangle|^2 + \iint |v_s^a|^2\langle|\eta(\boldsymbol{r}_s,t)|^2\rangle\,\rho_e(\boldsymbol{r}_s)\,\mathrm{d}\boldsymbol{r}_s, \qquad (36)$$

where $|v_s^a|^2\langle|\eta(\boldsymbol{r}_s,t)|^2\rangle$ is a symbolic notation to indicate the scattered wave energy at $\boldsymbol{r}_a$ due to a scatterer located at $\boldsymbol{r}_s$. From the expression for the coherent field of (35), and using the far-field approximation in the case of single scattering, (30) and (31), to evaluate the energy contribution from the scattered waves, (36) can be written as

$$\langle|\eta(x_a,t)|^2\rangle = (\tfrac{1}{2}AH)^2\left[1+|\alpha_c D(0)|^2+|\alpha_c D(\pi)|^2+\iint\frac{|D(\theta)|^2}{r_s}\rho_e(\boldsymbol{r}_s)\,\mathrm{d}\boldsymbol{r}_s\right]. \qquad (37)$$

Expressing $\mathrm{d}\boldsymbol{r}_s$ as $r_s\,\mathrm{d}r_s\,\mathrm{d}\theta$, (37) becomes

$$\langle|\eta(x_a,t)|^2\rangle = (\tfrac{1}{2}AH)^2\left[1+|\alpha_c D(0)|^2+|\alpha_c D(\pi)|^2+\beta\int_0^{2\pi}|D(\theta)|^2\,\mathrm{d}\theta\right], \qquad (38)$$

where

$$\beta = \lim_{r\to\infty}\int_0^r \rho_e(r_s)\,\mathrm{d}r_s. \qquad (39)$$

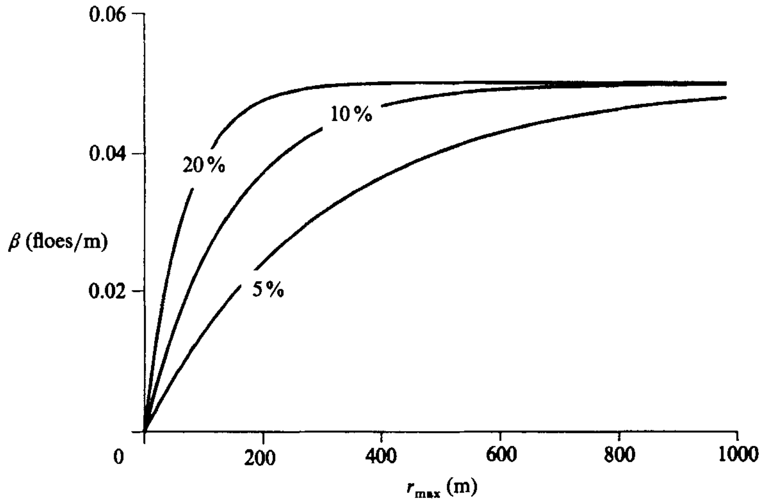

FIGURE 5. Energy factor, $\beta = \int_0^{r_{\max}} \rho_e(r)\,dr$, as a function of the distance of integration $r_{\max}$. Results are given for floes of radius $a = 10$ m and ice concentration, f_i, of 0.05, 0.1 and 0.2.

Allowing the energy contributions to come from scatterers located at distances of up to infinity (as in (39)), β tends to its asymptotic value of one floe per diameter, $1/2a$, whatever the ice concentration, f_i, is. If the scattering process is limited, in time for example, the upper limit of the integral in (39) takes a finite value, $r_{\max}$, which is the maximum distance travelled by the waves over a certain time interval Δt. In this situation, the influence of the degree of ice cover on β will be noticeable, β increasing with f_i (figure 5).

In (38), the incident wave energy, after scattering, is partitioned into: (i) a component identical to the unscattered incident wave, but of reduced (by the factor A) amplitude, $\frac{1}{2}AH$; (ii) energy associated with the two waves of the coherent field travelling in the $\pm$incident direction; (iii) directional scattering contributions with intensity apportioned as $|D(\theta)|^2$. When a wave spectrum, $F(f, \theta)$, is in the presence of an ice field, the energy of each spectral component is spread out over all directions, according to (38). The scattered spectrum is then obtained by summing, for each component, the contributions coming from waves of the same frequency and incident from all directions. Thus, for each frequency f_n, the spectrum after scattering, $F(f_n, \theta)$, is obtained by the product of the incident spectrum, $F^*(f_n, \theta)$, and a transfer function $[\boldsymbol{T}]_{f_n}$

$$F(f_n, \theta) = F^*(f_n, \theta)\,[\boldsymbol{T}]_{f_n}, \tag{40}$$

or, in tensor notation,

$$F(f_n, \theta_i) = F^*(f_n, \theta_j)\,(T_{ij})_{f_n}. \tag{41}$$

The matrix $[\boldsymbol{T}]_{f_n}$ is symmetric with each element $(T_{ij})_{f_n}$ of the form

$$(T_{ij})_{f_n} = A^2\{\beta|D(\theta_{ij})|^2\,\Delta\theta + \delta(\theta_{ij})\,(1+|\alpha_c D(0)|^2) + \delta(\pi-\theta_{ij})\,|\alpha_c D(\pi)|^2\}, \tag{42}$$

where $\theta_{ij} = |\theta_i - \theta_j|$, $\Delta\theta$ is the angular interval of the spectrum, δ is the Dirac function, and the parameters β, $|D(\theta_{ij})|^2$ and α are evaluated for the frequency $f = f_n$.

3.3. *Energy dissipation by the ice*

In §2, a dissipation term, S_{ds}, has been defined for the ice-free situation, where energy is lost mainly through wave breaking. When an ice cover is present, some energy is also lost within the ice field by various dissipative processes (ice deformation, wave

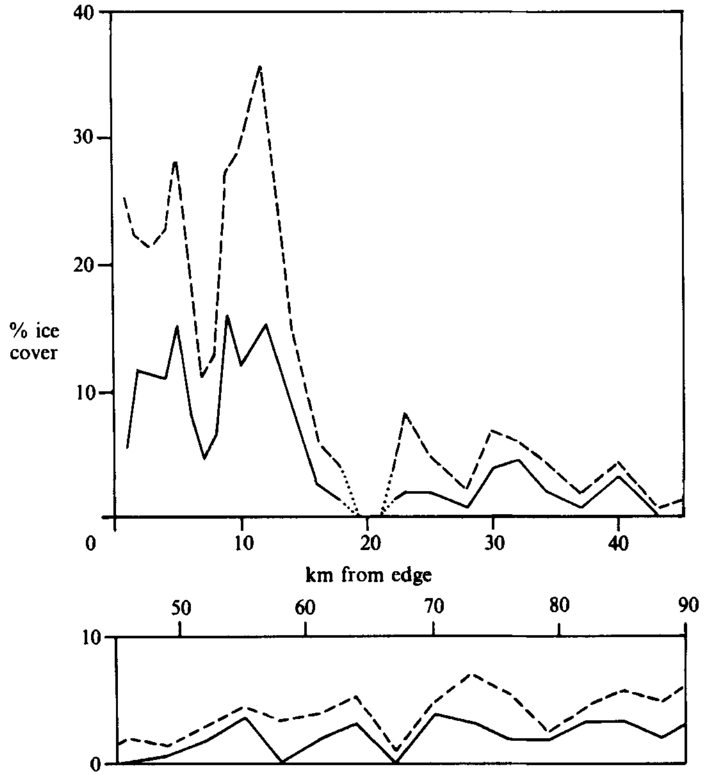

FIGURE 6. Percentage of sea surface covered by ice along laser track, June 6, 1972 (– – –, total cover; ——, floes > 20 m in diameter), (from Wadhams 1975).

breaking on the floes, etc.). By analogy to (24), where a scattering cross-section, σ_s, was defined, an absorption cross-section, σ_a, is introduced here to account for this extra dissipation.

The total energy associated with an incident wave of amplitude $\frac{1}{2}AH$ travelling through scatterers on a distance x, can be written in terms of this cross-section (e.g. Ishimaru 1978):

$$\langle|\eta(x,t)|^2\rangle = (\tfrac{1}{2}AH)^2 \exp(-\rho_0 \sigma_a x), \tag{43}$$

where ρ_0 is the number density without shading of (26). In order to evaluate the parameter σ_a, data collected by Wadhams (1975) off the east coast of Newfoundland have been examined. He measured, along a 90 km long line, the 'apparent' energy density for different frequency bands of swell entering the MIZ. Details of the degree of ice cover along the transect are given in figure 6 and the results are plotted in figure 7.

The transformation of the measured wavenumber spectrum into a frequency spectrum depends on the directional properties of the waves. In this case, the measurements were made along the major direction of the swell vector which was assumed to have no directional spread. If the energy of the swell is noticeably spread out over direction by the floes, the computed energy at a certain frequency becomes 'contaminated' by shorter waves travelling at an angle relative to the incident direction. Therefore, the spectral densities plotted in figure 7 are associated with the incident, non-scattered swell alone only in regions where the scattering by the ice

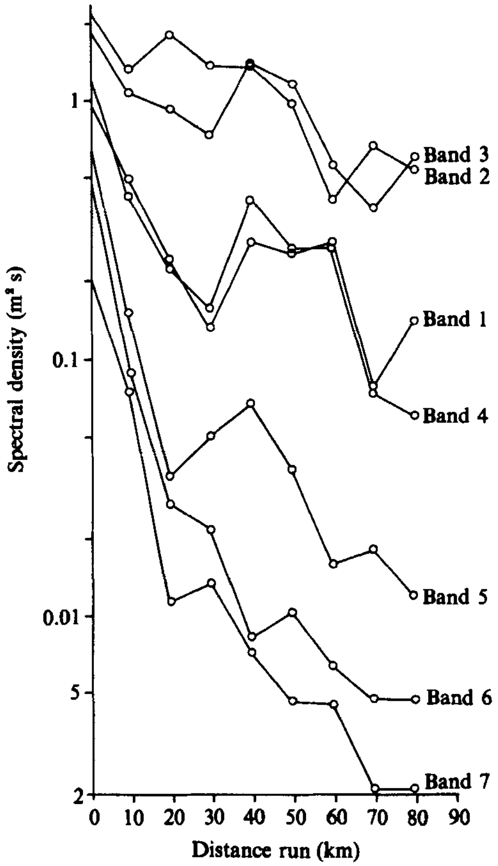

FIGURE 7. Energy density plotted against distance of penetration inside the ice field. Central period (s) for the bands: band 1, > 11.6; band 2, 11.6; band 3, 10.53; band 4, 9.35; band 5, 8.50; band 6, 7.85; band 7, 7.34 (from Wadhams 1975).

Band	T (s)	ka	σ_a(m)
1	?	?	0.070
2	11.6	0.21	0.012
3	10.53	0.25	0.033
4	9.35	0.32	0.088
5	8.50	0.39	0.148
6	7.85	0.46	0.149
7	7.34	0.53	0.146

TABLE 1. Absorption cross-sections computed from figure 7. Each band has a central period T.

floes is negligible, the incident swell remaining quasi-unidirectional, and can be used to estimate σ_a through (43).

In the outer 20 km, where a high fraction of the surface is covered by smaller floes, the assumption of unidirectionality appears reasonable, the parameter ka remaining small (see §4). Thus, in this region, the measured loss of energy can be attributed mainly to the absorption cross-section, and (43) should describe well, for each spectral component, the energy attenuation with distance. However, as one goes deeper into the ice cover, the proportion of larger floes gradually builds up and the scattering increases with ka. This causes an apparent increase of energy for a given band due to loss of unidirectionality at higher frequency (as seen in figure 7 for most bands at penetrations in excess of 20 km). Table 1 gives the computed absorption cross-sections for the first 20 km where $f_i \approx 0.15$ and $a \approx 7$ m. The value of σ_a rapidly increases to reach a maximum value of about 0.15 m. The data being limited, these results constitute a crude estimation of the absorption cross-section but provide a reasonable quantitative description that will be used in the model.

4. Results of floe response and scattering amplitudes

The wave-induced motion of a floating body is usually presented in the form of non-dimensional response amplitude operators (RAO) defined, here, as $\xi_b/\frac{1}{2}H$ for heave and surge, and $L\xi_3/180H$ for pitch (with ξ_3 in degrees). The response varies with the incident wavelength, the water depth, as well as the geometry and dimensions of the floe. The position of the centre of gravity and the radius of gyration (in pitch) are important factors in the determination of these RAOs. In order to compute these two parameters, a simplified density structure of the floe was assumed. The density of sea ice is not uniform throughout its thickness and varies owing to desalination as the floe ages. The floes present in the region described by the model are mainly composed of relatively young ice and the density is thus assumed uniform. Furthermore, due to the low thickness of the floes ($\leqslant 4$ m), the freeboard is expected to be small ($\leqslant 0.55$ m) (e.g. Tucker, Gow & Weeks 1987). The floes are thus considered, in the estimation of the position of the centre of gravity and the radius of gyration, to be completely submerged, with a uniform ice density equal to 1.

In figure 8, the computed RAOs are given as a function of ka for a floe of radius $a = 10$ m and draft $d = 3$ m. As indicated in the figure, the effect of water depth on the response is rather minor except for the low-frequency surge response. When the water depth changes from 30 m to 100 m, the heave and pitch peaks vary slightly in position and magnitude, but the response curves, for these two modes of motion, are almost unchanged. For the surge motion, the two curves are also closely related for low values of ka for which the shallow-water values are much larger. This can be explained by looking at how the water particle path changes with depth. When the diameter of the floe is small compared to the wavelength, the floe tends to behave essentially as a fluid particle (e.g. Lever, Reimer & Diemand 1984). For deep water waves, the water particle travels along closed circular orbits of radius $\frac{1}{2}H$, resulting in a surge RAO of 1. As the water depth to wavelength ratio decreases, the orbits become flat ellipses and the ratio $\xi_1/\frac{1}{2}H$ increases.

The typical heave response is shown in figure 9(a) where the RAOs are given for three floes of different thickness. For all three floes, the response is perfect (RAO→1) for long waves ($ka \to 0$) and shows very small movement in the short-wave region ($ka \gg 1$). In the intermediate range of ka, the floe geometry is critical in determining the importance of a resonant peak, which is absent for the thin floe, and increases in magnitude, narrows and slowly shifts to lower values of ka as the floe thickens.

As in the heave motion, the surge RAO indicates a perfect response for long waves and very small displacement for short waves (figure 9b). For intermediate values of ka, the response is generally larger for thinner floes which are moved by faster upper-layer flow. Also, when the radius-to-draft ratio decreases, a peak and a minimum develop. This feature is attributed in part to coupling between the pitch and surge

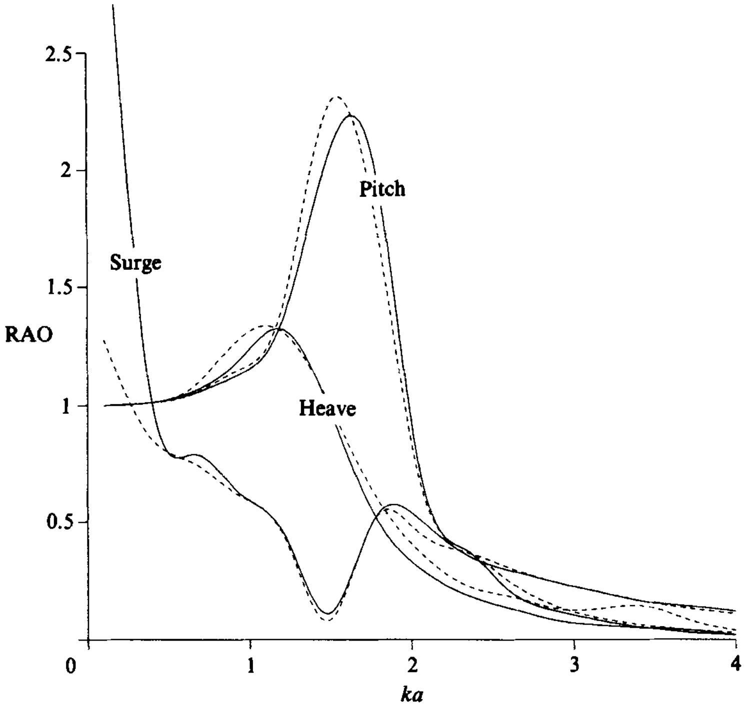

FIGURE 8. Response amplitude operators (RAO) for a floe of radius $a = 10$ m and draft $d = 3$ m. The RAOs are given for a depth of ——, 30 m; – – –, 100 m.

motions for which a 180° phase shift occurs simultaneously with the appearance of the peak (e.g. Wehausen 1971).

Again, the pitch response goes from near perfect response, following the wave slope, to negligible motion as *ka* increases (figure 9*c*). As in the heave motion, a resonant peak appears when the thickness of the floe increases. When the radius-to-draft ratio decreases, it narrows and its magnitude becomes more important, with its position shifting to lower *ka* values. No attempt has been made to include viscous pitch damping in the simulation. Its main effect would be to decrease the pitch resonant peak but, because the described floes have a rather high radius-to-draft ratio, the results predict a small resonant peak and, therefore, the viscous damping should remain minor.

Finally, the effect of the presence of a keel is examined. Real floes often present deformation features such as ridges and keels, due to intense wave activity or internal stress in the ice pack. The response of a cylindrical floe, to which has been appended a conical keel of 3 m in depth, is presented in figure 10. Although the keel modifies the motion by creating the effect of a slight increase in thickness, the overall characteristics of the response curves remain unchanged.

As seen in §3.2, the nature of the scattering amplitude, $D_b(\theta)$, determines the ability of a given icefield to disperse incident wave energy over all directions. For each of the three forced waves ($b = 1, 2, 3$), the summation in l of the general expression for $D_b(\theta)$, (23) or (A 11), leads to one single non-zero term: the $l = 0$ term for the heave motion corresponding to isotropic (uniform in all directions) waves, and the $l = 1$ term for surge and pitch with a simple $\cos\theta$ dependence of the scattered

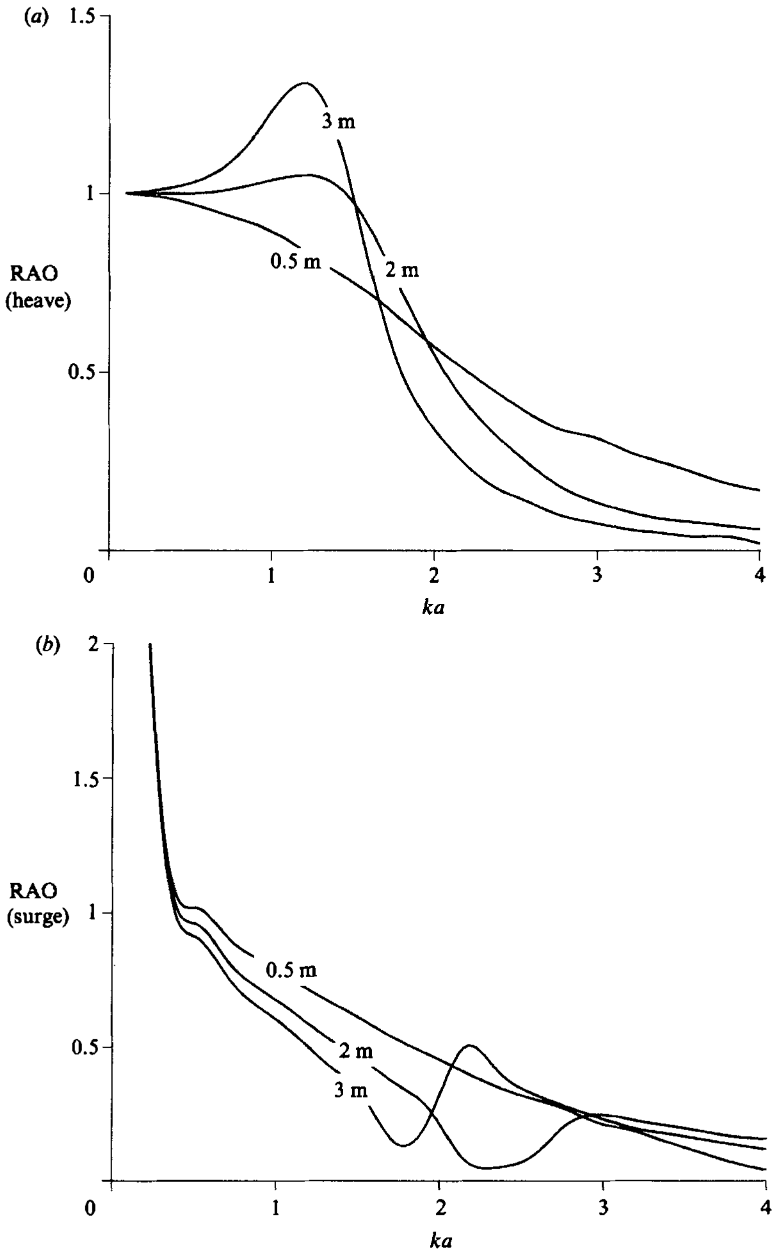

FIGURE 9(a, b). For caption see facing page.

waves. Also, the magnitude of the scattering amplitude, for each mode, is a combination of the dependence on the response amplitude operator, and of an increase, with the incident wavenumber, of the efficiency of the forced motions to generate waves. Figure 11 gives the RAO and the scattering cross-section,

$$Q_b = \int_0^{2\pi} |D_b(\theta)|^2 \, d\theta,$$

for a typical floe in surge, heave and pitch. In the low ka region, where the floe tends

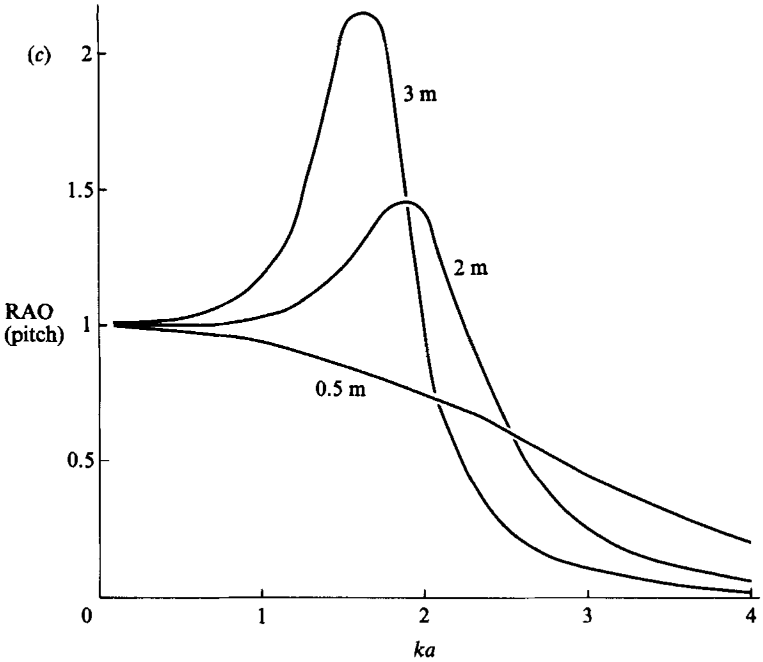

FIGURE 9. Response amplitude operators (RAO) in the (*a*) heave, (*b*) surge and (*c*) pitch motion, for floes of radius $a = 10$ m and draft $d = 0.5, 2, 3$ m, in a depth of 30 m.

to follow the water particle motion, there is very little energy associated with the forced waves. For intermediate values of ka, a marked increase of energy, accentuated by the presence of a resonant peak in heave and pitch, corresponds to scattered waves of considerable amplitude. Finally, in the short-wave region, the forced waves are of small height due to the vanishing forced motions. When the radius-to-draft ratio diminishes, the increased narrowness and the shift of the peak towards lower ka values result in an increasingly narrow peak for the cross-section, Q_b, for which the amplitude may even decrease. Although the heave and pitch RAO peaks are more developed for thicker floes, the wavenumber dependence of the cross-section minimizes their effect on the scattering ability of the floe.

For the diffraction scattering amplitude, $D_4(\theta)$, the summation in l has to be extended to a few terms ($l \approx 12$) such that the omitted terms do not contribute noticeably to the results. This produces a more complex directional distribution of the diffracted energy (figure 12). At the long wave limit, the small amplitude diffracted wave is almost perfectly isotropic. When ka increases, the outgoing wave separates into two parts: (i) the shadow-forming wave interfering with the incident wave to reduce the intensity behind the floe, and for which the energy concentrates into the incident direction as ka increases; (ii) the rest radiating out in other directions to form the reflected wave. For very large ka, the asymptotic value of the scattering cross-section (also called the effective width) is that for a circular cylinder, namely (e.g. Morse & Feshbach 1953, p. 1381)

$$\lim_{ka\to\infty} Q_4 = 4a. \tag{44}$$

For $ka \gg 1$, the object casts a geometrical shadow so that no energy is lost: half of the diffracted wave must cancel the incident wave for a width $2a$ behind the cylinder and the other half must be the reflected wave, with an effective width of $2a$. A

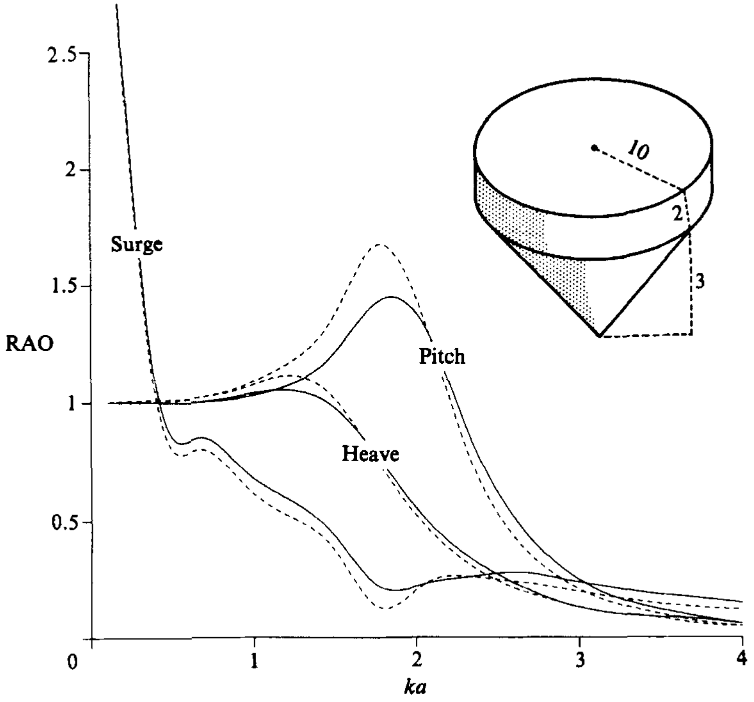

FIGURE 10. Response amplitude operators of a cylindrical floe ---, with and ——, without a keel. The floe has a radius $a = 10$ m and draft $d = 5$ m with a keel of 3 m in depth (water depth of 30 m).

convenient way to compute the diffraction cross-section, independent of the angular resolution of the model, is to use the forward-scattering theorem which, in this case, takes the form (Miles 1971).

$$Q_4 = -\left(\frac{8\pi}{k}\right)^{\frac{1}{2}} \operatorname{Re}\,(e^{\frac{1}{4}i\pi} D_4(0)). \tag{45}$$

The total scattering cross-section,

$$\sigma_s = \sum_{b=1}^{4} Q_b,$$

from which has been subtracted the incident direction contribution, $|D(0)|^2\,\Delta\theta$, measures the efficiency of the ice, for a given ka, to scatter energy away from the incident direction. By looking at the distribution of this corrected σ_s *vs.* ka, three distinct regimes can be identified: the 'small floe' regime for $ka \leqslant 1$; the 'efficient scattering' regime in the intermediate range of ka; and, finally, the 'backscattering' regime in the short wave region (figure 13).

For small $ka (ka \leqslant 1)$, the main contributions to the scattered waves come from the diffracted wave and from the wave forced by the heave motion. In that 'small floe' region, those two components are nearly isotropic and of small amplitude. Therefore, when the radius of the floe is small compared to the incident wavelength, only a small fraction of the incident energy is scattered (equally) in all directions.

For all floes, the ability of the ice cover to disperse energy increases considerably in the intermediate range of ka, but the extent and the nature of this 'efficient scattering' regime is a strong function of the geometry of the floes. Thin floes are 'good' scatterers over a broad range of $ka (1 \leqslant ka \leqslant 6)$, with a maximum in the region

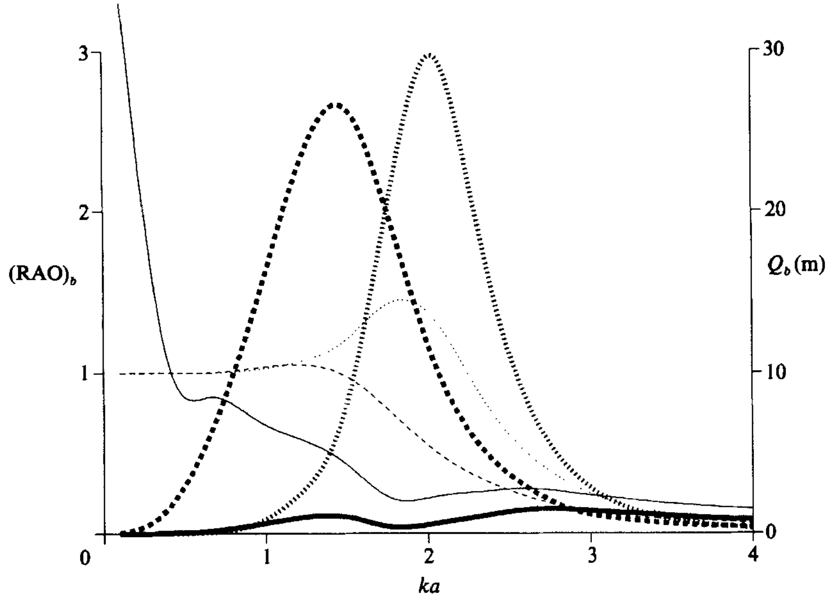

FIGURE 11. Response amplitude operators $(\mathrm{RAO})_b$, and scattering cross-sections, Q_b, for ——, surge; – – –, heave; and ..., pitch (the thick lines are for the cross-sections). The floe has a radius $a = 10$ m and draft $d = 2$ m in a water depth $h = 30$ m.

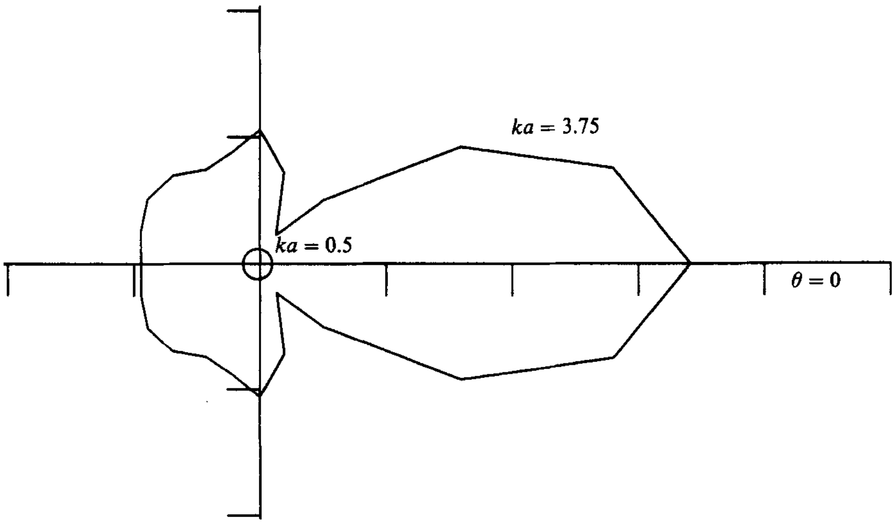

FIGURE 12. Diffraction differential scattering cross-section, $|D_4(\theta)|^2$, for $ka = 0.5$, 3.75. The floe has a radius $a = 10$ m and draft $d = 2$ m in a water depth $h = 30$ m.

where the incident wavelength is comparable to the floe diameter, owing to relatively large values of the pitch and heave RAOs where the forced motions are more efficacious in generating waves. As the radius-to-draft ratio decreases, the resonant heave and pitch RAO peaks shift to lower *ka* and the extent of this region, dominated by these two maxima, decreases $(1 \leqslant ka \leqslant 4)$.

When *ka* is large, only the diffraction contributes significantly to the scattered wave. In this 'backscattering' regime, as one approaches the limit $ka \rightarrow \infty$, about half

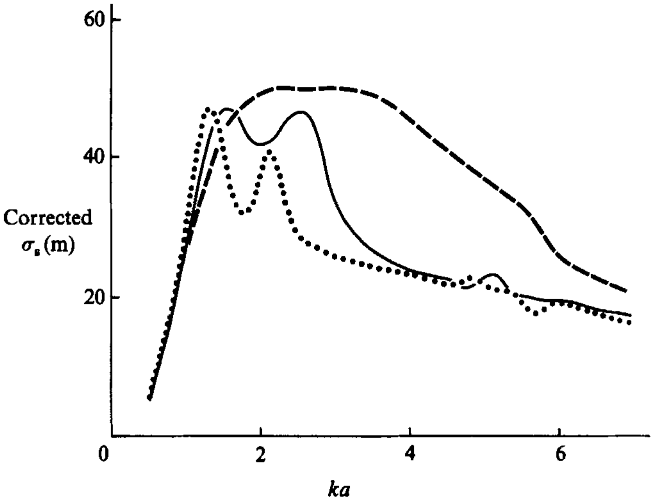

FIGURE 13. Total scattering cross-section corrected for the incident direction contribution, ($\sigma_s - |D(0)|^2\Delta\theta$), for floes of radius a = 10 m and draft d = ---, 0.5 m; ——, 2 m; ..., 3 m in a water depth h = 30 m.

of the diffracted energy is reflected backward, forming the backscattered wave, and the other half still travels in (or close to) the incident direction (resulting in a corrected σ_s of $2a$ m).

Although this is not the problem addressed here, it is interesting to interpret, with the help of these results, certain measurements of directional wave spectra entering the MIZ. Wadhams *et al.* (1986), during the MIZEX-84 experiment in the Greenland Sea, observed that the directionality of spectral components broadens significantly more rapidly for the high frequencies than for the swell frequencies. Knowing that the floe size gradually increases into the icefield, shorter waves are expected to be the first ones to enter the 'efficient scattering' regime and, consequently, their directional character is more rapidly affected. On the other hand, near the ice edge, the swell components propagate through small floes with negligible scattering. Further in the ice pack, as they encounter larger floes, these long waves eventually reach the 'efficient scattering' regime with their directionality seriously affected.

More recently, during an experiment in the Weddell Sea, Squire, Wadhams & Moore (1986) observed a marked change in the directional properties of the incident spectra which broadened to become isotropic at a point in the ice pack where the ice floes reached a size comparable to the wavelength of the spectral peak. Referring to figure 13, this would correspond to a maximum value for the corrected total cross-section near $ka = 3$ (appropriate for thin floes, $d = 0.5$ m).

5. Numerical integration procedure

Owing to the complexity of the different source functions in the energy balance equation (including the additional S_{ice} term), an important simplification is introduced by assuming the medium unbounded and uniform. This reduces the problem to the evolution of purely time-limited waves owing to the elimination of the advective term, $C_g \cdot \nabla F$, of (4) which then takes the form

$$\frac{\mathrm{d}F(f,\theta;t)}{\mathrm{d}t} = (S_{\text{in}}+S_{\text{ds}})(1-f_i)+S_{\text{nl}}+S_{\text{ice}}, \tag{46}$$

with S_{ice} introduced in (51) in the form of a transfer function. The numerical integration of (46) proceeds following a simple first-order forward difference method. At first, timesteps are set to very small values ($\Delta t \approx 10$ s) to account for the rapid initial change in spectral shape (reported in §6.2). Once this process is stabilized, timesteps are dynamically adjusted, starting with $(\Delta t)_n = t_{n-1}/5$ and reducing it by a factor 2 in case of a too large $\Delta F/F$. The spectrum is specified for frequencies distributed according to $f_n = f_0(1.1)^{n-1}$, with $f_0 = 0.07$ Hz being the lowest frequency, up to $2.5 \times f_{\text{peak}}$ (where f_{peak} represents the frequency at the maximum of the spectrum). Beyond this value, a high-frequency f^{-5} decay is assumed, adjusted independently for each direction. There is an ongoing debate on the exact nature of the high-frequency spectral region, with strong evidence for an f^{-4} dependence (e.g. Donelan, Hamilton & Hui 1985; Phillips 1985). However, the choice of an f^{-5} shape in the short-wave region of the spectrum is not important for this analysis. The angular resolution of the spectrum is 30°.

The initial wave field specified is a JONSWAP spectrum (Hasselmann *et al.* 1973) of the form

$$F(f,\theta) = \frac{\alpha g^2}{(2\pi)^4 f^5}\exp\left[-\frac{5}{4}\left(\frac{f}{f_{\text{peak}}}\right)^{-4}\right]\gamma^{\exp\left[-\frac{(f-f_{\text{peak}})^2}{2\sigma^2 f_{\text{peak}}^2}\right]}G(f,\theta), \tag{47}$$

where

$$\sigma = \begin{cases} 0.07 & \text{for } f \leqslant f_{\text{peak}}, \\ 0.09 & \text{for } f > f_{\text{peak}}. \end{cases}$$

Here the parameter α is equivalent to the usual Phillips' constant but with a time dependence, $\gamma = 3.3$ is the peak enhancement factor and $G(f,\theta)$ a directional spreading function. For a certain initial time t_0(s), the values of α and f_{peak} are obtained from the results of the parametric model of Hasselmann *et al.* (1976):

$$f_{\text{peak}} = \frac{16.8g}{U_{10}}\left(\frac{gt_0}{U_{10}}\right)^{-\frac{3}{7}} \tag{48}$$

and

$$\alpha = 0.033\left(\frac{f_{\text{peak}}U_{10}}{g}\right)^{\frac{2}{3}} \tag{49}$$

where U_{10} is the wind at 10 m.

The spreading function, in (47), is of the cosine-power type and takes the form used by Hasselmann & Hasselmann (1985*b*)

$$G(f,\theta) = I(p)\cos^{2p}(\tfrac{1}{2}\theta), \tag{50}$$

where

$$p = 10^{0.99}\left(\frac{f}{f_{\text{peak}}}\right)^{\kappa},$$

$$\kappa = \begin{cases} 4.06 & \text{for } f < f_{\text{peak}}, \\ -2.34 & \text{for } f \geqslant f_{\text{peak}}. \end{cases}$$

The normalization factor is given by

$$I(p) = \frac{2^{2p-1}\Gamma^2(p+1)}{\pi\Gamma(2p+1)},$$

with Γ the Gamma function.

At each timestep, S_{in}, S_{ds} and S_{nl} are computed to obtain a new spectrum which is then modified, for each frequency f_n, by the scattering transfer function of (40):

$$F(f_n,\theta;t+\Delta t) = [F(f_n,\theta;t)+((S_{\mathrm{in}}+S_{\mathrm{ds}})(1-f_{\mathrm{i}})+S_{\mathrm{nl}})\Delta t]\,[\boldsymbol{T}]_{f_n} \tag{51}$$

where, in $[\boldsymbol{T}]_{f_n}$, the value of β is determined by setting the upper limit of integration $r_{\max} = C_{\mathrm{g}}\Delta t$ in (39).

The energy factor A, introduced in (23), is obtained, for each frequency, from energy conservation applied to (38), taking the loss of energy through the absorption cross-section, σ_{a}, into account:

$$A = \left(1+|\alpha_{\mathrm{c}}D(0)|^2+|\alpha_{\mathrm{c}}D(\pi)|^2+\beta\int_0^{2\pi}|D(\theta)|^2\,\mathrm{d}\theta+f_d\right)^{-\frac{1}{2}}, \tag{52}$$

where f_d, the fraction of energy lost in the scattering process, is given by

$$f_d = (\exp(\rho_0\sigma_{\mathrm{a}}C_{\mathrm{g}}\Delta t)-1). \tag{53}$$

The integration procedure is repeated for a series of timesteps until dominant trends can be clearly established.

6. Time integration of wave spectra

6.1. *Ice-free situation*

The numerical integration of (46) was first performed, for calibration purposes, for the more common case of an ice-free ocean surface ($f_{\mathrm{i}} = 0$), in a water depth $h = 30$ m. A wind of $U_{10} = 10$ m/s was assumed to have been blowing for about 3.25 h ($t_0 = 11700$ s) which, according to (48), corresponds to a JONSWAP spectrum with an initial peak frequency $f_{\mathrm{peak}} = 0.3$ Hz. Figure 14 shows the initial one-dimensional (integrated over direction θ) energy balance. The input and dissipation terms are maximum at the peak, according to their linear dependence on the spectrum. The more complex nonlinear term, S_{nl}, has its typical three-lobed distribution; the energy is transferred from the central region of the spectrum to both shorter and longer wave components. The nonlinear transfer is the principal source of energy on the low-frequency forward face of the spectrum, and controls the shape of the spectrum including the position and development of the peak itself. The two-dimensional nonlinear term, $S_{\mathrm{nl}}(f,\theta)$, has a broader directional distribution in its high-frequency lobe than in the two other lobes, and the low-frequency lobe is confined to a narrow frequency band and directional distribution (figure 15). There are also, near the peak frequency, two relative maxima (a, a') in directions at an angle to the wind, as previously discussed by several authors (Webb 1978; Fox 1976; Longuet-Higgins 1976).

The integration was performed over a short duration of about 1.4 h. Throughout the integration, the angular distribution of the spectrum could be satisfactorily described by the initial spreading function of (50). The evolution of the total energy, E, and the peak frequency, f_{peak}, is shown in figure 16 together with the predictions of the parametric wave model of Hasselmann *et al.* (1976). In the latter, which is based on measurements of fetch-limited wave spectra from various sources (including JONSWAP results), the evolution of f_{peak} and E is obtained from (48) and (49) using the relation

$$\frac{Ef_{\mathrm{peak}}^4}{g^2\alpha} = 1.6\times10^{-4}. \tag{54}$$

The decrease of the peak frequency predicted by the model closely follows the

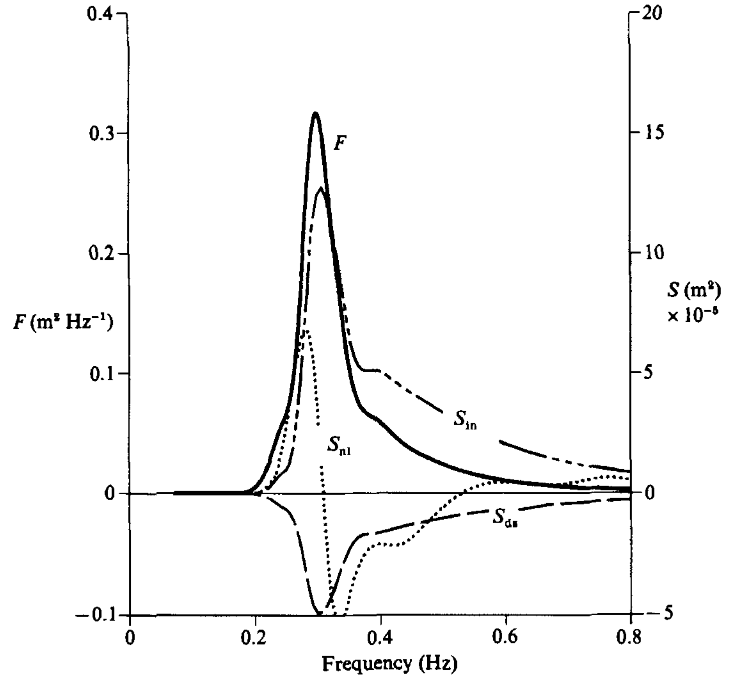

FIGURE 14. One-dimensional energy balance for a JONSWAP spectrum with $f_{\text{peak}} = 0.3$ Hz. The wind blows at $U_{10} = 10$ m/s on an ice-free ocean (F, frequency spectrum; S_{in}, wind input; S_{ds}, dissipation; S_{nl}, nonlinear interactions).

parametric model predictions. The total energy increases at about the same rate for the two models, but with an initial disagreement on the absolute value of the energy, E. This difference, although not important, can be explained by the discrepancy between (54), used in the parametric model to relate the total energy of the spectrum to the parameter α, and the relationship obtained from the numerical integration of a JONSWAP spectrum (like the one used here to describe the initial sea state), namely (Carter 1982):

$$\frac{E f_{\text{peak}}^4}{g^2 \alpha} = 1.957 \times 10^{-4}. \tag{55}$$

6.2 *Effect of a partial ice cover*

The evolution of the spectrum, used in the previous section to describe the initial sea state ($t_0 = 11700$ s), is now examined under the action of a partial ice cover. The integration was performed for two different ice concentrations (10% and 20%) with floes of radius $a = 10$ m and draft $d = 2$ m, and a wind $U_{10} = 10$ m/s. The resulting spectra, $F(f, \theta)$, are contoured in figure 17(a) and figure 17(b), for the first 12 min of the integration.

In both cases, the ice cover appears to be very efficient in spreading out the wave energy over all directions. The results of §4 indicate that most of the energy of the initial spectrum is contained in the efficient scattering regime ($1 \leqslant ka \leqslant 4$), with the high-frequency components extending into the backscattering regime ($ka \geqslant 4$). Accordingly, on the spectral forward face and at the peak, the spectrum becomes almost instantaneously isotropic, and, in the less energetic high-frequency region, the energy is scattered more slowly and preferentially in the backward direction, resulting in the gradual build-up of a secondary maximum near $\theta = \pm 180°$.

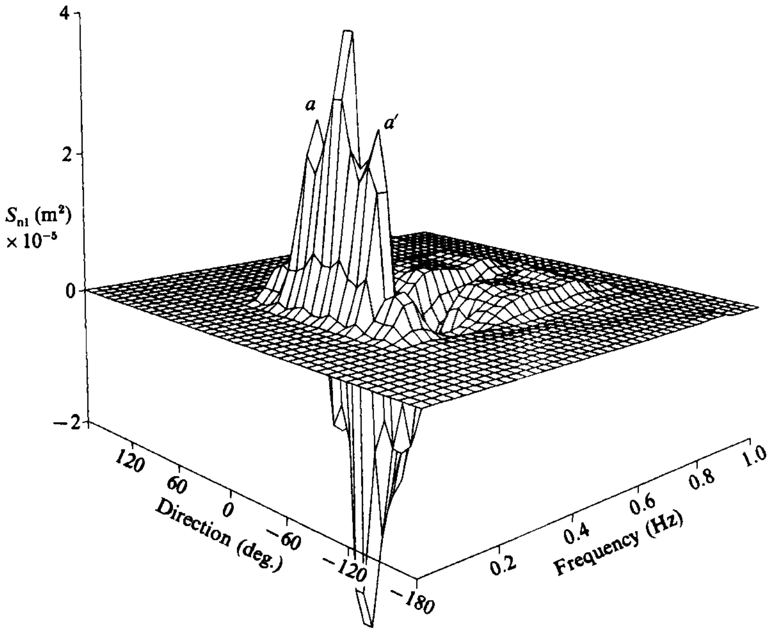

FIGURE 15. Two-dimensional nonlinear term, $S_{nl}(f, \theta)$, for a JONSWAP spectrum with $f_{peak} = 0.3$ Hz.

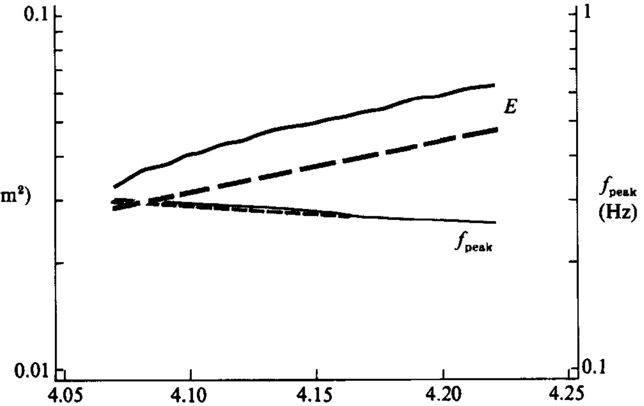

FIGURE 16. Time-limited growth curves for the total energy, E, and the peak frequency, f_{peak}. The wind blows at 10 m/s over an ice-free ocean (——, model predictions; ---, Hasselmann's parametric model).

As the spectrum rapidly tends to isotropy, the one-dimensional energy balance is drastically modified. Figure 18 shows the new energy balance obtained after only 12 min, with an ice cover of 20%. Here, S_{ice} represents the energy loss due to the ice, through the fraction f_d of (53). The extra dissipation caused by the ice is now an important term in the energy balance with, in this case, a magnitude of about twice that of the S_{ds} term at the peak. Furthermore, the wind input term, S_{in}, has decreased to less than half of its ice-free value (see figure 14). Although this term is reduced to 80% of its previous value by the $(1-f_i)$ factor in (46), the calculated decrease is mainly due to the actual nature of the parameterization of the wind input.

In (5), the $((U_5 \cos\theta/c)-1)$ term ensures that the energy is transferred from the atmosphere to the waves in proportion to the phase velocity component in the direction of the wind, and at a rate proportional to the energy which they already have. As the wave energy is scattered by the floes away from the wind direction, the energy input rapidly diminishes. This reduction in the input function, combined with the extra dissipation of the energy by the ice, severely limits the growth of the spectral energy content. The rate at which the energy is supplied by the wind rapidly becomes insufficient to overcome the energy lost through the different dissipation processes, and the energy decays (figure 19).

The nonlinear transfer is also seriously affected as the spectral shape changes. It still has its typical three-lobed shape but with considerably reduced amplitude and larger directional spread (figure 20). This known dependence of the nonlinear exchange mechanism on the angular spectral distribution (e.g. Hasselmann & Hasselmann 1981, 1985*a*) was first discussed by Hasselmann (1963). He found that, since most of the energy flux is due to interactions in regions of high energy density, an increase in angular spread explains the associated decrease in energy transfer. In our problem, where the energy is being scattered away from the mean direction, the energy transfer effectively decreases and becomes relatively inefficient in shifting the peak towards lower frequencies. Thus, a partial ice cover reduces the shift of the spectral peak towards longer waves (figure 21).

The ice concentration, f_i, does not appear to be a critical parameter in the scattering process. The energy decay rate is affected by a change in f_i due to the factor $(1-f_i)$ added in the balance equation and to the variation of the attenuation rate in (43). However, as f_i varies from 0.05 to 0.25, the scattering ability of the ice cover remains relatively unchanged, the parameter β of (38) presenting only small variations (see figure 5). Therefore, a small change in ice concentration of a noticeable ice cover ($f_i \geqslant 0.05$), within the range of validity of the model ($f_i \leqslant 0.25$), does not significantly affect the spectral evolution obtained, the characteristic timescale of the scattering mechanism (time needed for an incident spectrum to become isotropic) being so small relative to the ones of the other energy terms modifying the spectrum.

The evolution of a spectrum with the same peak frequency ($f_{\text{peak}} = 0.3$ Hz), but generated by a stronger wind, $U_{10} = 20$ m/s, is then examined with a 20% ice cover, $f_i = 0.2$. Equations (48) and (49) gives an initial time $t_0 \approx 1.3$ h and a more sharply peaked initial spectrum, with $\alpha = 0.024$. As for the lower wind velocity, the spectrum rapidly tends to isotropy, the characteristic timescale of the scattering process remaining relatively small (≈ 15 min). Because of the higher wind speed, the dissipation takes longer to overcome the input from the atmosphere but, as the spectrum becomes isotropic, the energy balance rapidly adjusts to limit the wave growth both in length and height (figure 22).

The integration is then done from an initial JONSWAP spectrum with $f_{\text{peak}} = 0.4$ Hz, describing a younger sea state ($t_0 \approx 1.7$ h for $U_{10} = 10$m/s). In this case, only the low-frequency spectral region, near the forward face of the spectrum, is contained in the efficient scattering regime, the rest of the frequencies extending over the backscattering region. Consequently, the spectrum undergoes differential scattering, with the low frequencies becoming rapidly isotropic and the short-wave tail being nearly unaffected (except for the formation of the backscattered 'bump') (figure 23). Since an important portion of the energetic region of the spectrum is scattered away from the mean direction, the wind input function and the nonlinear energy transfer are reduced by the scattering, but not as much as in the previous case with the smaller f_{peak}. Thus, the spectrum is, at first, allowed to grow, but at a rate smaller

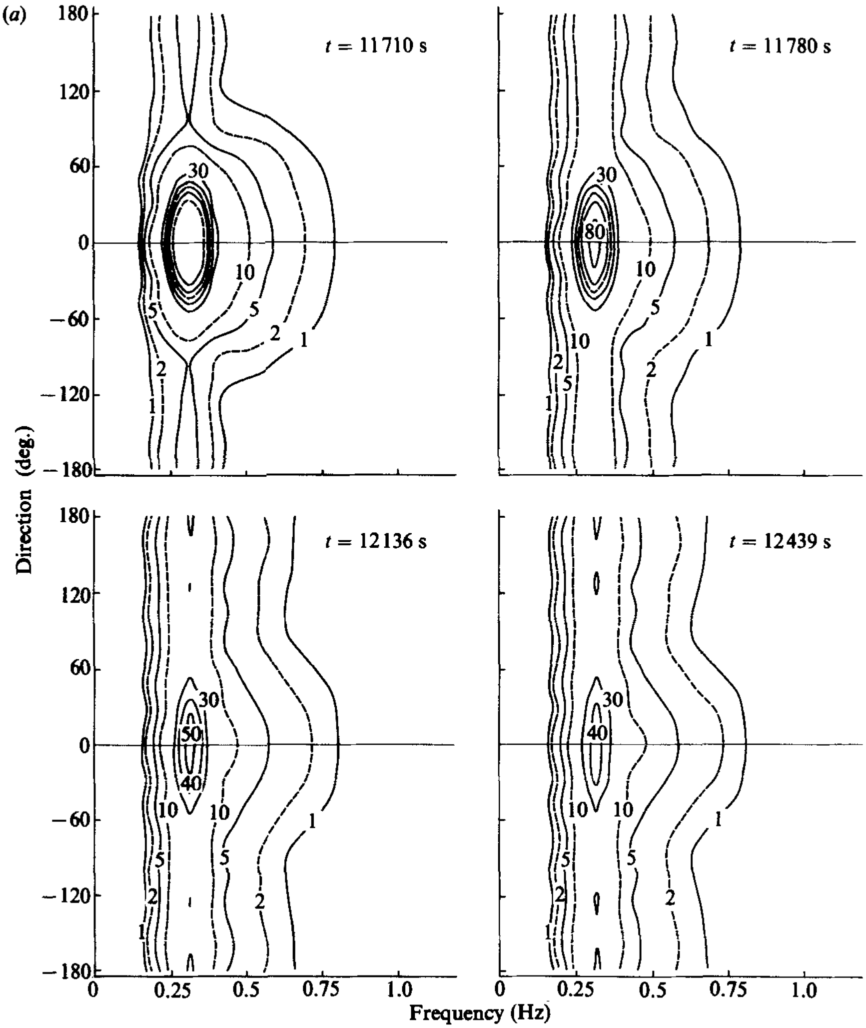

FIGURE 17(*a*). For caption see facing page.

than in the ice-free situation. However, as the peak slowly shifts towards lower frequencies, the energy transferred to the spectral forward face is rapidly spread out over all directions, resulting in the same growth-limited situation as before.

So far, in all cases studied, where an important fraction of the energy was spread out by the efficient scattering regime, the ice cover caused a very rapid tendency towards spectral isotropy, leading to a decay of the wave energy. This raises an important question: 'Is there a minimum wind speed for which waves can still grow in the presence of a certain ice cover?' The evolution of a JONSWAP spectrum, with $f_{\text{peak}} = 0.3$ Hz and $\alpha = 0.014$ (as in the $U_{10} = 10$ m/s case), initially isotropic, is examined under different wind conditions. There is a minimum wind speed for which the initial energy balance of such a spectrum results in an increase of the total energy ($(U_{10})_{\text{min}} \approx 16$ m/s for $f_i = 0.2$; $(U_{10})_{\text{min}} \approx 13$ m/s for $f_i = 0.1$). However, because of the important reduction of the nonlinear energy transfer predicted by the model, these waves no longer grow in length. Thus, at first, as the wind transfers energy to the wave field, these short waves rapidly reach the maximum steepness at which they

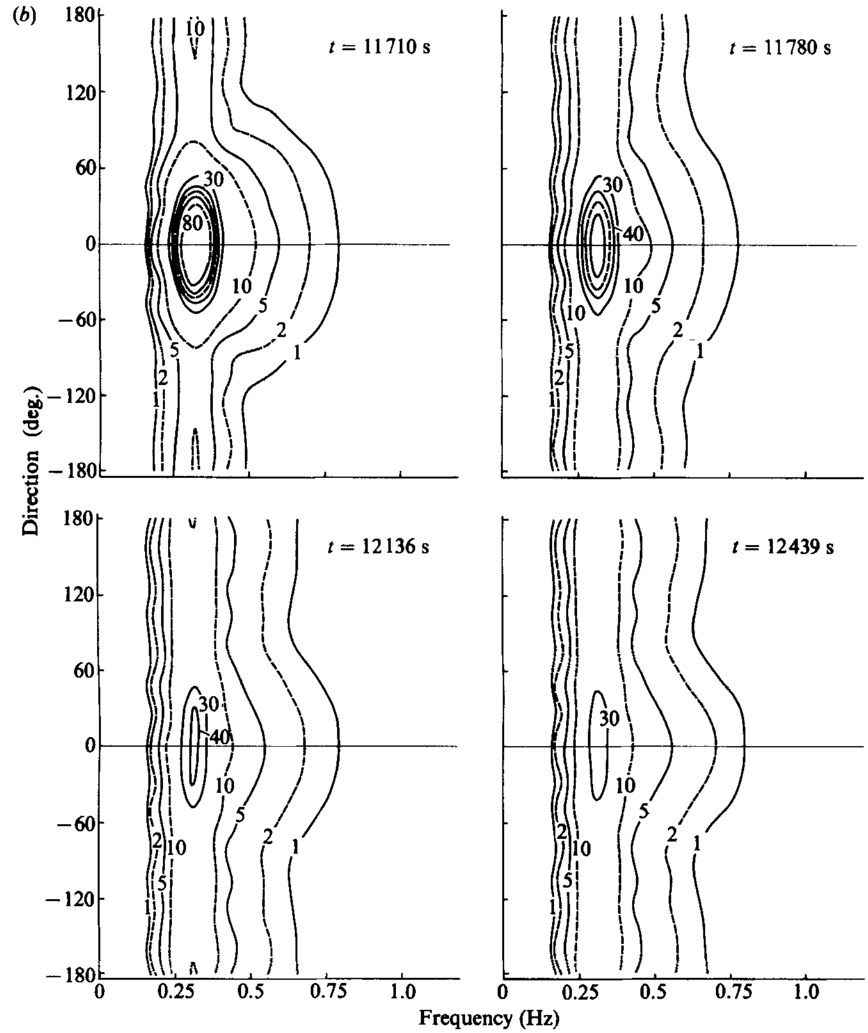

FIGURE 17. Time evolution of the spectrum, $F(f,\theta)$ (10^{-3} $\mathrm{m^{-2}\,s\,rad^{-1}}$), in the presence of a partial ice cover of (*a*) 10% and (*b*) 20% with ice floes of radius $a = 10$ m and draft $d = 2$ m, $U_{10} = 10$ m/s and $f_{\mathrm{peak}}(t_0) = 0.3$ Hz.

lose their energy through breaking. In other words, the spectral growth of an isotropic spectrum is limited by the S_{ds} quadratic dependence on the wave-steepness parameter, $\hat{\alpha}$ (see (6)). The total energy of the spectrum rapidly reaches a saturation level at which the three active energy terms, S_{in}, S_{ds} and S_{ice}, balance each other. Since the fraction of energy lost due to the ice, in a timestep Δt, depends on the wave frequency (through C_g of (53)), each spectral component is attenuated by the ice at a different rate, the longer waves decaying faster. Consequently, the average frequency of the spectrum, $\bar{\omega}$, increases with time. Although this is beneficial to the wind input term, through a decrease of the average wave speed c, the associated higher value of the wave-steepness parameter $\hat{\alpha}$, which varies as $\bar{\omega}^{4}$, causes a more important increase of the S_{ds} term. Therefore, from the saturation level, the energy of the wave field diminishes with time, as the average frequency increases under the action of the selective S_{ice} term (figure 24). Continuing the integration, since the

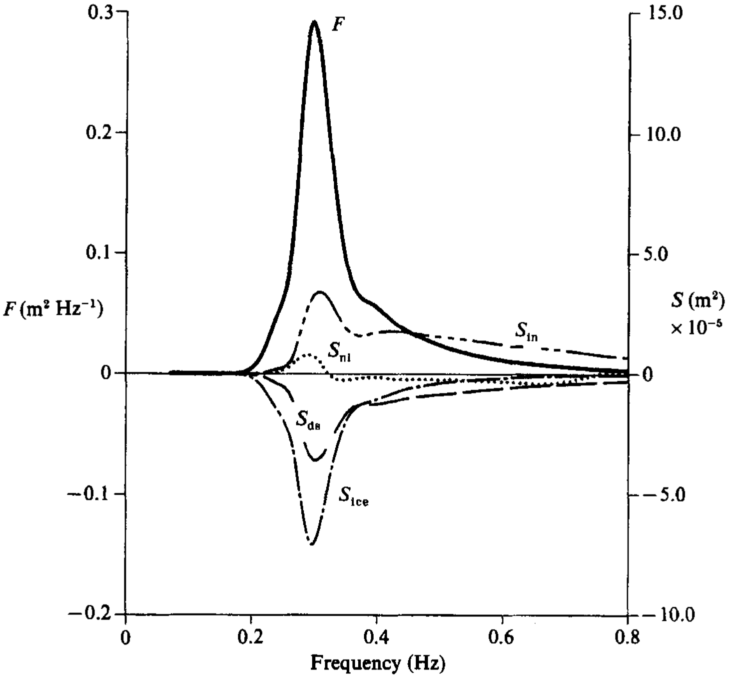

FIGURE 18. One-dimensional energy balance at $t \approx (t_0 + 12)$ min, with an ice concentration. $f_i = 0.2$ and $f_{\text{peak}}(t_0) = 0.3$ Hz.

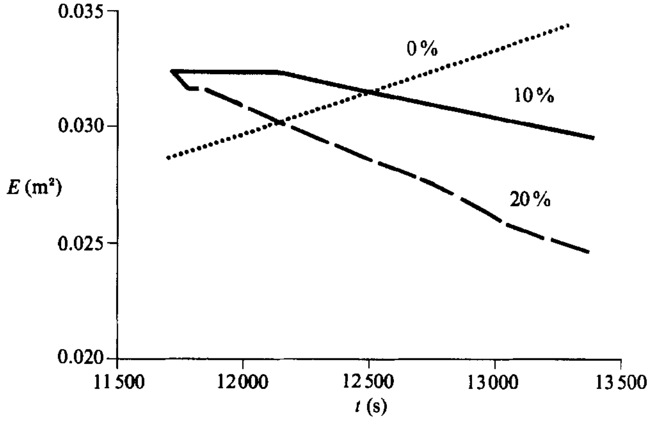

FIGURE 19. Time evolution of the total energy, E, of an initial JONSWAP spectrum ($f_{\text{peak}} = 0.3$ Hz) in the presence of an ice cover of 0% (from the Hasselmann parametric model), 10% and 20%, with a wind $U_{10} = 10$ m/s.

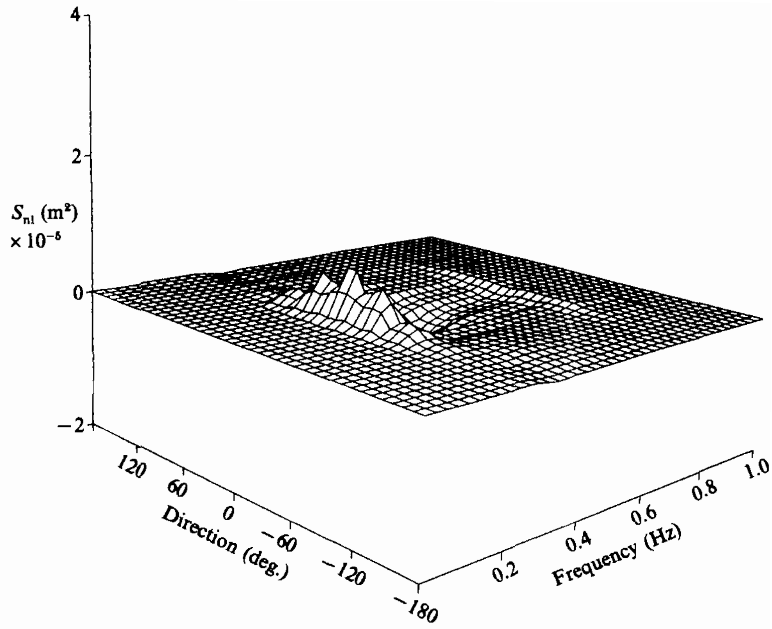

FIGURE 20. Two-dimensional nonlinear term, $S_{nl}(f, \theta)$, at $t \approx (t_0 + 12)$ min, with an ice concentration $f_i = 0.2$ (see figure 15 for the $f_i = 0$ situation).

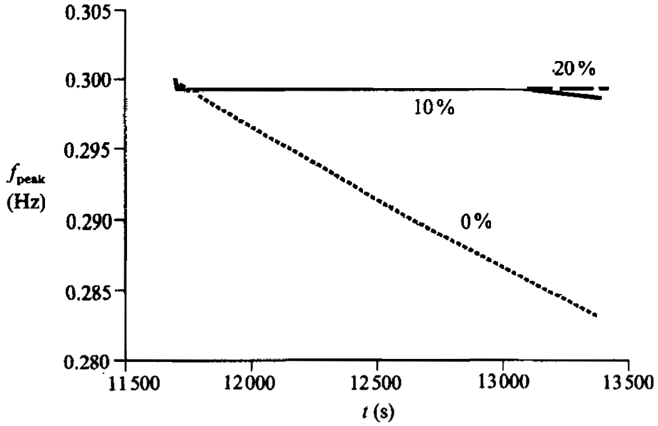

FIGURE 21. Time evolution of the peak frequency, f_{peak}, of an initial JONSWAP spectrum (f_{peak} = 0.3 Hz) in the presence of a partial ice cover of 0 % (from the Hasselmann parametric model), 10 % and 20 %.

parameter $\hat{\alpha}$ also depends on the energy content E, the wind input could again balance the dissipation, but at very low energy levels (for $E < 0.0124$ m², in the problem of figure 24) corresponding to waves of negligible amplitude. Thus, in this time-limited situation, even with a wind speed high enough to cause an initial wave growth, the spectral energy rapidly decreases to very low values.

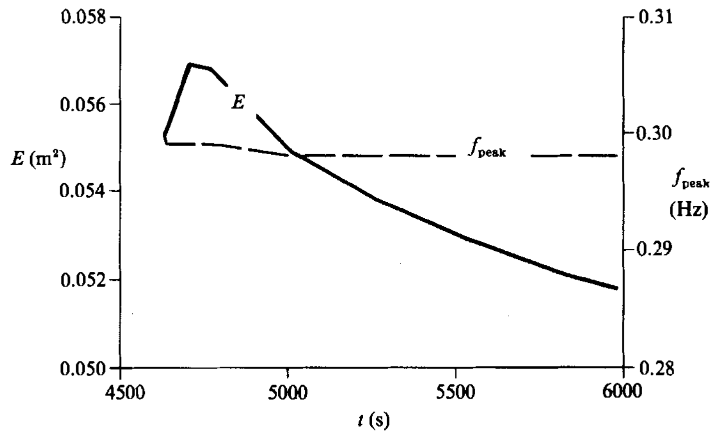

FIGURE 22. Time evolution of the peak frequency, f_{peak}, and total energy, E, for an initial JONSWAP spectrum ($f_{\text{peak}} = 0.3$ Hz) in the presence of a partial ice cover of 20% with a wind $U_{10} = 20$ m/s.

7. Discussion of the initial wave generation problem

All the integrations described so far have been done with a certain non-zero initial wave field suddenly in presence of an ice cover, and, obviously, do not describe the problem of initial wave generation from a calm ocean surface. However, the results presented above can be used to better understand the problem of wave generation by an offshore wind starting to blow over the MIZ. As soon as the ice cover becomes sparser, the wind begins to generate very short fetch limited waves for which a high value of ka locates them in the backscattering region. Although some of the energy is lost in the backward direction, the waves are allowed to grow, but at a rate smaller than in the ice-free situation. However, as those waves travel further along the fetch, their wavenumbers decrease and, likewise, the floes gradually become smaller. Thus, the parameter ka associated with these waves diminishes as they approach the ice edge. In the most favourable conditions (strong wind blowing over a long fetch covered by a low ice concentration of large floes), waves of relatively important wavelength could eventually develop. But, as they would approach the ice edge, these waves would encounter smaller floes ($a \leqslant 10$ m), and the resulting ka ($(k_{\text{peak}} a) \leqslant 6$, for $L_{\text{peak}} \geqslant 10$ m) would cause, through scattering, a rapid inhibition of the wave growth. If the wind speed is larger than the $(U_{10})_{\min}$ required to initially sustain wave growth, the spectral energy would quickly reach a saturation level where the dissipation would balance the wind input to the waves, and the total energy of the spectrum would be restricted to relatively low values. Otherwise, the energy of the wave field would rapidly decay to a level at which the reduced energy input to these short waves would balance the dissipation terms. In both situations, the energy of the spectrum would be restrained to low values by the partial ice cover. Therefore, according to the model results, an offshore wind blowing over the outer part of the MIZ, cannot generate a substantial wave field, the surface waves remaining short, of small amplitude and with a large directional spread.

In examining the model results, it is important to keep in mind its limitations. For example, the assumption of a uniform ice cover does not properly describe all situations in the MIZ. It is very common to encounter large polynyas in which regular short fetch wave generation is possible. As suggested by Wadhams (1983),

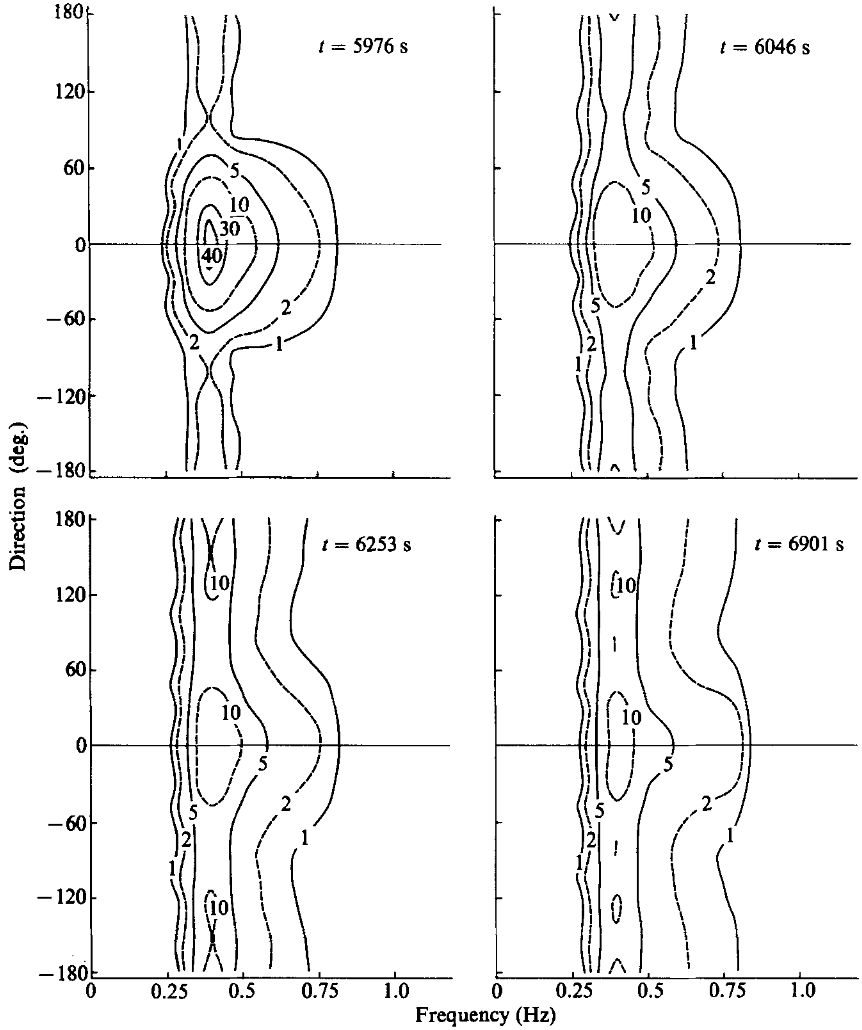

FIGURE 23. Time evolution of the spectrum, $F(f,\theta)\,(10^{-3}\ \mathrm{m^2\,s\,rad^{-1}})$, in the presence of a partial ice cover of 20% with ice floes of radius $a = 10$ m and draft $d = 2$ m, $U_{10} = 10$ m/s and $f_{\mathrm{peak}}(t_0) = 0.4$ Hz.

these waves could play, through wave radiation pressure, an important role in the formation of ice edge bands frequently observed, especially in the Bering Sea.

We wish to thank Dr M. de St Q. Isaacson for the use of his wave-floating structure program, Dr P. Wadhams, Dr K. Hasselmann and his wife, S. Hasselmann, for useful discussions concerning different aspects of this project and the use of S. Hasselmann's wave model. The Natural Sciences and Engineering Research Council provided support for this project in the form of a strategic grant to P.H.L. and a scholarship to D.M.

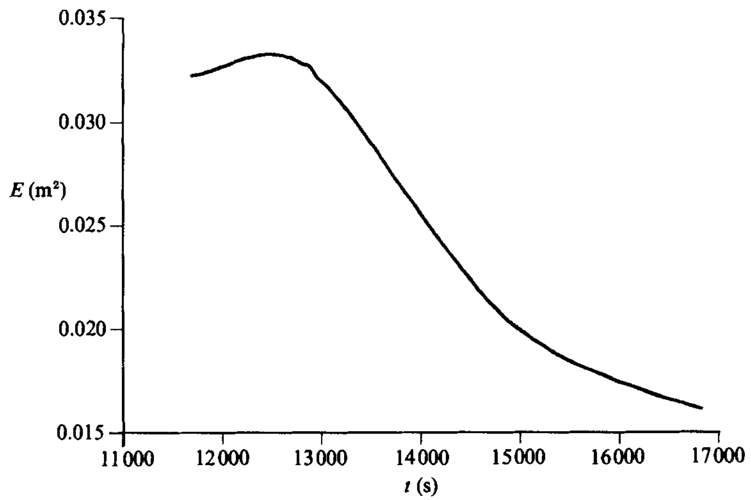

FIGURE 24. Time evolution of the total energy, E, of an initially isotropic spectrum with $f_{\mathrm{peak}}(t_0) = 0.3$ Hz, $f_i = 0.2$, and $U_{10} = 16$ m/s.

Appendix. Scattering amplitudes in infinite depth

In deep water, the appropriate form for the Green function of (14) is (John 1950), with appropriate corrections on signs, in agreement with Wehausen & Laitone 1960,

$$G(x, X) = \frac{1}{R'} - \int_0^\infty \frac{\nu+\mu}{\nu-\mu} \mathrm{e}^{(z+Z)\mu} J_0(\mu q)\,\mathrm{d}\mu, \tag{A 1}$$

where
$$R' = ((x-X)^2+(y-Y)^2+(z-Z)^2)^{\frac{1}{2}},$$
$$q = ((x-X)^2+(y-Y)^2)^{\frac{1}{2}},$$

$\nu = \omega^2/g$, and the path of integration runs below the root ν of the denominator. At large distance from the floe, John (1950) showed that this equation reduces to

$$\lim_{q\to\infty} G(x, X) = 2\pi \mathrm{i}\, k \mathrm{e}^{k(z+Z)}\, H_0^{(1)}(kq) + O(1/q^3) \tag{A 2}$$

where $H_0^{(1)}$ is the Hankel function of the first kind of order 0. It is convenient to convert (A 2) to cylindrical coordinates with

$$r^2 = x^2+y^2, \quad R^2 = X^2+Y^2, \quad \tan\theta = \frac{y}{x}, \quad \tan\Theta = \frac{Y}{X};$$

then
$$q^2 = R^2+r^2-2rR\cos(\theta-\Theta). \tag{A 3}$$

Equation (A 2) can now be transformed in a symmetrical form, in the same way that Fenton (1978) obtained (15) in the finite-depth case. The use of Graf's addition theorem (e.g. Abramowitz & Stegun 1965) gives

$$H_0^{(1)}(kq) = \sum_{l=-\infty}^{\infty} H_l^{(1)}(kr)\, J_l(kR) \cos[l(\theta-\Theta)]. \tag{A 4}$$

In this series, the $-l^{th}$ term is equal to the l^{th} term. Thus, introducing a Kronecker delta, (A 4) can be written as

$$H_0^{(1)}(kq) = \sum_{l=0}^{\infty} (2-\delta_{l0})\, H_l^{(1)}(kr)\, J_l(kR) \cos[l(\theta-\Theta)]. \tag{A 5}$$

Substituting this new form for the Hankel function into (A 2), the deep-water Green function, for large r, is given by

$$\lim_{r\to\infty} G = 2\pi \mathrm{i}\, k \mathrm{e}^{k(z+Z)} \sum_{l=0}^{\infty} (2-\delta_{l0}) \cos[l(\theta-\Theta)]\, J_l(kR)\, H_l^{(1)}(kr) + O(r^{-3}). \qquad \text{(A 6)}$$

Substituting (A 6) and (17) into (14), the scattered far-field potentials, for $b = 1, \ldots 4$, take the form:

$$\phi_b(r,\theta,z) \approx \frac{1}{4\pi} \int_{S_0} \sum_{l=0}^{\infty} f_{bl}(s) \cos(l\Theta)\, G_l (2-\delta_{l0}) \cos[l(\theta-\Theta)]\, \mathrm{d}S, \qquad \text{(A 7)}$$

with $$G_l = 2\pi \mathrm{i}\, k \mathrm{e}^{k(z+Z)} J_l(kR)\, H_l^{(1)}(kr).$$

As in the finite depth case, $\mathrm{d}S$ is expressed as $R\,\mathrm{d}\Theta\,\mathrm{d}s$ and the equilibrium contour, s_0, discretized into N segments of length L_j:

$$\phi_b(r,\theta,z) \approx \frac{1}{4\pi} \sum_{j=1}^{N} \sum_{l=0}^{\infty} f_{bl}(s_j)\, G_l(r, R_j, z, Z_j) \int_0^{2\pi} (2-\delta_{l0}) \cos(l\Theta) \times \cos[l(\theta-\Theta)]\, \mathrm{d}\Theta\, R_j L_j. \qquad \text{(A 8)}$$

Integrating over Θ, (A 8) reduces to

$$\phi_b(r,\theta,z) \approx \frac{1}{2} \sum_{j=1}^{N} \sum_{l=0}^{\infty} f_{bl}(s_j)\, G_l(r, R_j, z, Z_j) \cos(l\theta)\, R_j L_j. \qquad \text{(A 9)}$$

From known asymptotic formulae for the Hankel functions (e.g. Abramovitz & Stegun 1965), it follows that, for large r, the far-field approximation of (A 9) can be written as

$$\phi_b(r,\theta,z) = \left\{ (2\pi k)^{\frac{1}{2}} \mathrm{i} \exp(-\tfrac{1}{4}\mathrm{i}\pi) \sum_{j=1}^{N} \sum_{l=0}^{\infty} f_{bl}(s_j) \exp(k(z+Z_j))\, J_l(kR_j) \times \exp(-\tfrac{1}{2}\mathrm{i}\pi l)\, R_j L_j \cos(l\theta) \right\} \frac{1}{r^{\frac{1}{2}}} \exp(\mathrm{i}kr) + O(r^{-\frac{3}{2}}). \qquad \text{(A 10)}$$

Finally, the surface displacement, far enough from the floe, is obtained from the far-field potential at the surface ($z = 0$), using the linearized surface boundary condition. As in the case of finite depth, it takes the form of outgoing cylindrical waves:

$$\eta_b(r,\theta,t) = \mathrm{Re}\left(\tfrac{1}{2} A H D_b'(\theta) \frac{1}{r^{\frac{1}{2}}} \mathrm{e}^{\mathrm{i}(kr-\omega t)} \right), \qquad \text{(A 11)}$$

with, in this case,

$$D_b'(\theta) = -\frac{\omega}{g} \frac{\xi_b}{\frac{1}{2}H} (2\pi k)^{\frac{1}{2}} \exp(-\tfrac{1}{4}\mathrm{i}\pi) \sum_{j=1}^{N} \sum_{l=0}^{\infty} f_{bl}(s_j) \exp(kZ_j)\, J_l(kR_j) \exp(-\tfrac{1}{2}\mathrm{i}\pi l)\, R_j L_j \cos(l\theta)$$

for $b = 1, 2, 3$, and

$$D_b'(\theta) = -\frac{\omega}{g} \frac{1}{\frac{1}{2}H} (2\pi k)^{\frac{1}{2}} \exp(-\tfrac{1}{4}\mathrm{i}\pi) \sum_{j=1}^{N} \sum_{l=0}^{\infty} f_{bl}(s_j) \exp(kZ_j)\, J_l(kR_j) \exp(-\tfrac{1}{2}\mathrm{i}\pi l)\, R_j L_j \cos(l\theta)$$

for $b = 4$.

REFERENCES

Abramowitz, M. & Stegun, I. A. 1965 *Handbook of Mathematical Functions*. Dover.

Allender, J. H., Barnett, T. P., Bertotti, L., Bruinsma, J., Cardone, V. J., Cavaleri, L., Ephraums, J. J., Golding, B., Greenwood, A., Guddal, J., Günther, H., Hasselmann, K., Hasselmann, S., Joseph, P., Kawai, S., Komen, G. J., Lawson, L., Linné, H., Long, R. B., Lybanon, M., Maeland, E., Rosenthal, W., Toba, Y., Uji, T. & Voogt, W. J. P. de 1985 Sea Wave Modeling Project (SWAMP). An intercomparison study of wind wave prediction models, Part 1: Principal results and conclusions. *Ocean Wave Modeling*. Plenum, 256 pp.

Bauer, J. & Martin, S. 1980 Field observations of the Bering sea ice edge properties during March 1979. *Mon. Weather Rev.* **108**, 2045–2056.

Carter, D. J. T. 1982 Prediction of wave height and period for a constant wind velocity using the JONSWAP results. *Ocean Engng* **9**, 17–33.

Donelan, M. A., Hamilton, J. & Hui, W. H. 1985 Directional spectra of wind-generated waves. *Phil. Trans. R. Soc. Lond.* A **315**, 509–562.

Fenton, J. D. 1978 Wave forces on vertical bodies of revolution. *J. Fluid Mech.* **85**, 241–255.

Fox, M. J. H. 1976 On the nonlinear transfer of energy in the peak of a gravity-wave spectrum II. *Proc. R. Soc. Lond.* A **348**, 467–483.

Garrison, C. J. 1978 Hydrodynamic loading of large offshore structures: three-dimensional source distribution methods. In *Numerical Methods in Offshore Engineering* (ed. O. C. Zienkiewicz, R. V. Lewis & K. G. Stagg), pp. 87–140. Wiley.

Golding, B. 1983 A wave prediction system for real-time sea state forecasting. *Q. J. R. Met. Soc.* **109**, 393–416.

Hasselmann, K. 1960 Grundgleichungen der Seegangsvoraussage. *Schiffstechnik.* **7**, 191–195.

Hasselmann, K. 1962 On the non-linear energy transfer in a gravity-wave spectrum. Part 1. General theory. *J. Fluid Mech.* **12**, 481–500.

Hasselmann, K. 1963 On the non-linear energy transfer in a gravity-wave spectrum. Part 3. Evaluation of the energy flux and swell-sea interaction for a Newmann spectrum. *J. Fluid Mech.* **15**, 385–398.

Hasselmann, K. 1974 On the spectral dissipation of ocean waves due to white capping. *Boundary-Layer Met.* **6**, 107–127.

Hasselmann, K., Barnett, T. P., Bouws, E., Carlson, H., Cartwright, D. E., Enke, K., Ewing, J. A., Gienapp, H., Hasselmann, D. E., Kruseman, P., Meerburg, A., Müller, P., Olbers, D. J., Richter, K., Sell, W. & Walden, H. 1973 Measurements of wind-wave growth and swell decay during the Joint North Sea Wave Project (JONSWAP). *Deutsch. Hydrogr. Z.* A **8** (12), 95 pp.

Hasselmann, K., Ross, D. B., Müller, P. & Sell, W. 1976 A parametric wave prediction model. *J. Phys. Oceanogr.* **6**, 200–228.

Hasselmann, S. & Hasselmann, K. 1981 A symmetrical method of computing the nonlinear transfer in a gravity-wave spectrum. *Hamb. Geophys. Einzelschriften* A **52**, 138 pp.

Hasselmann, S. & Hasselmann, K. 1985*a* Computations and parameterizations of the nonlinear energy transfer in a gravity wave spectrum. Part I: A new method for efficient computations of the exact nonlinear transfer integral. *J. Phys. Oceanogr.* **15**, 1369–1377.

Hasselmann, S. & Hasselmann, K. 1985*b* Computations and parameterizations of the nonlinear energy transfer in a gravity wave spectrum. Part II: Parameterizations of the nonlinear energy transfer for application in wave models. *J. Phys. Oceanogr.* **15**, 1378–1391.

Isaacson, M. de St Q. 1982 Fixed and floating axisymmetric structures in waves. *J. Waterway, Port, Coastal and Ocean Div. ACCE* **108** (WW2), 180–199.

Ishimaru, A. 1978 *Wave Propagation and Scattering in Random Media. Volume* 2 *Multiple Scattering, Turbulence, Rough Surfaces, and Remote Sensing*. Academic. 310 pp.

Janssen, P. A. E. M., Komen, G. J. & Voogt, W. J. P. de 1984 An operational coupled hybrid wave prediction model. *J. Geophys. Res.* **89** (C3), 3635–3654.

Jeffreys, H. 1962 *Asymptotic Approximations*. Oxford University Press. 144 pp.

John, F. 1950 On the motion of floating bodies, II. Simple harmonic motions. *Commun. Pure Appl. Maths* **3**, 45–101.

KOMEN, G. J., HASSELMANN, S. & HASSELMANN, K. 1984 On the existence of a fully developed wind-sea spectrum. *J. Phys. Oceanogr.* **14**, 1271–1285.

LEVER, J. H., REIMER, E. & DIEMAND, D. 1984 A model study of the wind-induced motion of small icebergs and bergy bits. *Proc. Third Intl. Offshore Mechanics and Arctic Engng Symp.* vol. 3, pp. 282–290.

LONGUET-HIGGINS, M. S. 1976 On the nonlinear transfer of energy in the peak of a gravity-wave spectrum: a simplified model. *Proc. R. Soc. Lond.* A **347**, 311–328.

MASSON, D. 1987 Spectral evolution of wind generated surface gravity waves in a dispersed ice field. PhD thesis, The University of British Columbia. 95 pp.

MILES, J. W. 1971 A note on variational principles for surface-wave scattering. *J. Fluid Mech.* **46**, 141–149.

MORSE, P. M. & FESHBACH, H. 1953 *Methods of Theoretical Physics. Part II.* McGraw-Hill. 979 pp.

PHILLIPS, O. M. 1960 On the dynamics of unsteady gravity waves of finite amplitude. Part 1. The elementary interactions. *J. Fluid Mech.* **9**, 193–217.

PHILLIPS, O. M. 1985 Spectral and statistical properties of the equilibrium range in wind-generated gravity waves. *J. Fluid Mech.* **156**, 505–531.

ROBIN, G. DE Q. 1963 Wave propagation through fields of pack ice. *Phil. Trans. R. Soc.* A **255**, 313–339.

SARPKAYA, T. & ISAACSON, M. 1981 *Mechanics of Wave Forces on Offshore Structures.* Van Nostrand Reinhold. 651 pp.

SNYDER, R. L., DOBSON, F. W., ELLIOTT, J. A. & LONG, R. B. 1981 Array measurements of atmospheric pressure fluctuations above surface gravity waves. *J. Fluid Mech.* **102**, 1–59.

SQUIRE, V. A. 1983 Numerical modelling of realistic ice floes in ocean waves. *Ann. Glaciol.* **4**, 277–282.

SQUIRE, V. A. 1984 A theoretical, laboratory, and field study of ice-coupled waves. *J. Geophys. Res.* **89** (C5), 8069–8079.

SQUIRE, V. A., WADHAMS, P. & MOORE, S. C. 1986 Surface gravity wave processes in the winter Weddell Sea. *AGU fall meeting report, EOS* **67** (44), 1005.

TUCKER, W. B., GOW, A. J. & WEEKS, W. F. 1987 Physical properties of summer sea ice in the Fram strait. *J. Geophys. Res.* **92** (C7), 6787–6803.

WADHAMS, P. 1973 Attenuation of swell by sea ice. *J. Geophys. Res.* **78** (18), 3552–3563.

WADHAMS, P. 1975 Airborne laser profiling of swell in an open ice field. *J. Geophys. Res.* **80** (33), 4520–4528.

WADHAMS, P. 1978 Wave decay in the marginal ice zone measured from a submarine. *Deep-Sea Res.* **25**, 23–40.

WADHAMS, P. 1983 A mechanism for the formation of ice edge bands. *J. Geophys Res.* **88** (C5), 2813–2818.

WADHAMS, P. 1986 The seasonal ice zone. In *The Geophysics of Sea Ice* (ed. N. Untersteiner), pp. 825–991. Plenum.

WADHAMS, P., SQUIRE, V. A., EWING, J. A. & PASCAL, R. W. 1986 The effect of the marginal ice zone on the directional wave spectrum of the ocean. *J. Phys. Oceanogr.* **16**, 358–376.

WEBB, D. J. 1978 Non-linear transfers between sea waves. *Deep-Sea Res.* **25**, 279–298.

WEHAUSEN, J. V. 1971 The motion of floating bodies. *Ann. Rev. Fluid Mech.* **3**, 237–268.

WEHAUSEN, J. V. & LAITONE, E. V. 1960 *Surface waves, Encyclopedia of physics*, Fluid Dynamics III, 9, (ed. S. Flugge), pp. 446–778. Springer.